The Astrophysical Journal, 998:6 (29pp), 2026 February 10 https://doi.org/10.3847/1538-4357/ae25f0

Time-dependent Modeling of the Subhour Spectral Evolution during the 2013 Outburst of Mrk 421

K. Abe[1], S. Abe[2], J. Abhir[3], A. Abhishek[4], A. Aguasca-Cabot[5], I. Agudo[6], T. Aniello[7], S. Ansoldi[8,9], L. A. Antonelli[7], A. Arbet Engels[10,49], C. Arcaro[11], T. T. H. Arnesen[12], A. Babić[13], C. Bakshi[14], U. Barres de Almeida[15], J. A. Barrio[16], L. Barrios-Jiménez[12], I. Batković[11], J. Baxter[2], J. Becerra González[12], W. Bednarek[17], E. Bernardini[11], J. Bernete[18], A. Berti[10], C. Bigongiari[7], A. Biland[3], O. Blanch[19], G. Bonnoli[7], Ž. Bošnjak[13], E. Bronzini[7], I. Burelli[19], A. Campoy-Ordaz[20], A. Carosi[7], R. Carosi[21], M. Carretero-Castrillo[5], A. J. Castro-Tirado[6], D. Cerasole[22], G. Ceribella[10], Y. Chai[2], A. Cifuentes[18], J. L. Contreras[16], J. Cortina[18], S. Covino[7,23], F. D'Ammando[24], P. Da Vela[7], F. Dazzi[7], A. De Angelis[11], B. De Lotto[8], R. de Menezes[15], J. Delgado[19,25], C. Delgado Mendez[18], F. Di Pierro[26], R. Di Tria[22], L. Di Venere[22], A. Dinesh[16], D. Dominis Prester[27], A. Donini[7], D. Dorner[28], M. Doro[11], L. Eisenberger[28], D. Elsaesser[29], J. Escudero[6], L. Fariña[19], L. Foffano[7], L. Font[20], S. Fröse[29], Y. Fukazawa[30], R. J. García López[12], S. García Soto[18], M. Garczarczyk[31], S. Gasparyan[32], J. G. Giesbrecht Paiva[15], N. Giglietto[22], F. Giordano[22], P. Gliwny[17], T. Gradetzke[29], R. Grau[19], D. Green[10], J. G. Green[10], P. Günther[28], A. Hahn[10], T. Hassan[18], L. Heckmann[10,33], J. Herrera Llorente[12], D. Hrupec[34], D. Israyelyan[32], J. Jahanvi[8], I. Jiménez Martínez[10], J. Jiménez Quiles[19], J. Jormanainen[35], S. Kankkunen[35], T. Kayanoki[30], J. Konrad[29], P. M. Kouch[35], G. Koziol[36], H. Kubo[2], J. Kushida[1], M. Láinez[16], A. Lamastra[7], E. Lindfors[35], S. Lombardi[7], F. Longo[8,37], M. López-Moya[16], A. López-Oramas[12], S. Loporchio[22], L. Lulić[27], E. Lyard[36], P. Majumdar[14], M. Makariev[38], M. Mallamaci[39], G. Maneva[38], M. Manganaro[27], S. Mangano[18], K. Mannheim[28], S. Marchesi[7], M. Mariotti[11], M. Martínez[19], P. Maruševec[13], S. Menchiari[6], J. Méndez Gallego[6], S. Menon[7,40], D. Miceli[11], J. M. Miranda[4], R. Mirzoyan[10], M. Molero González[12], E. Molina[12], H. A. Mondal[2], A. Moralejo[19], C. Nanci[7], A. Negro[26], V. Neustroev[41], L. Nickel[29], M. Nievas Rosillo[12], C. Nigro[19], L. Nikolić[4], S. Nozaki[2], A. Okumura[42], J. Otero-Santos[11], S. Paiano[7], D. Paneque[10,49], R. Paoletti[4], J. M. Paredes[5], M. Peresano[10], M. Persic[8,43], M. Pihet[6], G. Pirola[10], F. Podobnik[4], P. G. Prada Moroni[21], E. Prandini[11], W. Rhode[29], M. Ribó[5], J. Rico[19], A. Roy[30], N. Sahakyan[32], F. G. Saturni[7], K. Schmitz[29], F. Schmuckermaier[10], T. Schweizer[10], A. Sciaccaluga[7], G. Silvestri[11], A. Simongini[7], J. Sitarek[17], V. Sliusar[36], D. Sobczynska[17], A. Stamerra[7], J. Strišković[34], D. Strom[10], M. Strzys[2], Y. Suda[30], H. Tajima[42], R. Takeishi[2], F. Tavecchio[7], T. Terzić[27], M. Teshima[2,10], A. Tutone[7], S. Ubach[20], J. van Scherpenberg[10], M. Vazquez Acosta[12], S. Ventura[4], G. Verna[4], I. Viale[26], A. Vigliano[8], C. F. Vigorito[26], E. Visentin[26], V. Vitale[44], I. Vovk[2], R. Walter[36], F. Wersig[29], M. Will[10], T. Yamamoto[45], P. K. H. Yeung[2]
(MAGIC Collaboration),
M. Petropoulou[46,47,49], M. Polkas[48,49], and A. Mastichiadis[46]

[1] Japanese MAGIC Group: Department of Physics, Tokai University, Hiratsuka, 259-1292 Kanagawa, Japan
[2] Japanese MAGIC Group: Institute for Cosmic Ray Research (ICRR), The University of Tokyo, Kashiwa, 277-8582 Chiba, Japan
[3] ETH Zürich, CH-8093 Zürich, Switzerland
[4] Università di Siena and INFN Pisa, I-53100 Siena, Italy
[5] Universitat de Barcelona, ICCUB, IEEC-UB, E-08028 Barcelona, Spain
[6] Instituto de Astrofísica de Andalucía-CSIC, Glorieta de la Astronomía s/n, 18008, Granada, Spain
[7] National Institute for Astrophysics (INAF), I-00136 Rome, Italy
[8] Università di Udine and INFN Trieste, I-33100 Udine, Italy
[9] International Center for Relativistic Astrophysics (ICRA), Rome, Italy
[10] Max-Planck-Institut für Physik, D-85748 Garching, Germany
[11] Università di Padova and INFN, I-35131 Padova, Italy
[12] Instituto de Astrofísica de Canarias and Dpto. de Astrofísica, Universidad de La Laguna, E-38200, La Laguna, Tenerife, Spain
[13] Croatian MAGIC Group: University of Zagreb, Faculty of Electrical Engineering and Computing (FER), 10000 Zagreb, Croatia
[14] Saha Institute of Nuclear Physics, A CI of Homi Bhabha National Institute, Kolkata 700064, West Bengal, India
[15] Centro Brasileiro de Pesquisas Físicas (CBPF), 22290-180 URCA, Rio de Janeiro (RJ), Brazil
[16] IPARCOS Institute and EMFTEL Department, Universidad Complutense de Madrid, E-28040 Madrid, Spain
[17] University of Lodz, Faculty of Physics and Applied Informatics, Department of Astrophysics, 90-236 Lodz, Poland
[18] Centro de Investigaciones Energéticas, Medioambientales y Tecnológicas, E-28040 Madrid, Spain
[19] Institut de Física d'Altes Energies (IFAE), The Barcelona Institute of Science and Technology (BIST), E-08193 Bellaterra (Barcelona), Spain
[20] Departament de Física, and CERES-IEEC, Universitat Autònoma de Barcelona, E-08193 Bellaterra, Spain
[21] Università di Pisa and INFN Pisa, I-56126 Pisa, Italy
[22] INFN MAGIC Group: INFN Sezione di Bari and Dipartimento Interateneo di Fisica dell'Università e del Politecnico di Bari, I-70125 Bari, Italy
[23] Como Lake centre for AstroPhysics (CLAP), DiSAT, Universitá dell'Insubria, via Valleggio 11, 22100, Como, Italy
[24] INAF Istituto di Radioastronomia, Via P. Gobetti 101, I-40129 Bologna, Italy
[25] Port d'Informació Científica (PIC), E-08193 Bellaterra (Barcelona), Spain
[26] INFN MAGIC Group: INFN Sezione di Torino and Università degli Studi di Torino, I-10125 Torino, Italy
[27] Croatian MAGIC Group: University of Rijeka, Faculty of Physics, 51000 Rijeka, Croatia
[28] Universität Würzburg, D-97074 Würzburg, Germany
[29] Technische Universität Dortmund, D-44221 Dortmund, Germany
[30] Japanese MAGIC Group: Physics Program, Graduate School of Advanced Science and Engineering, Hiroshima University, 739-8526 Hiroshima, Japan
[31] Deutsches Elektronen-Synchrotron (DESY), D-15738 Zeuthen, Germany

[32] Armenian MAGIC Group: ICRANet-Armenia, 0019 Yerevan, Armenia
[33] Université Paris Cité, CNRS, Astroparticule et Cosmologie, F-75013 Paris, France
[34] Croatian MAGIC Group: Josip Juraj Strossmayer University of Osijek, Department of Physics, 31000 Osijek, Croatia
[35] Finnish MAGIC Group: Finnish Centre for Astronomy with ESO, Department of Physics and Astronomy, University of Turku, FI-20014 Turku, Finland
[36] University of Geneva, Chemin d'Ecogia 16, CH-1290 Versoix, Switzerland
[37] Dipartimento di Fisica, Università di Trieste, I-34127 Trieste, Italy
[38] Institute for Nuclear Research and Nuclear Energy, Bulgarian Academy of Sciences, BG-1784 Sofia, Bulgaria
[39] INFN MAGIC Group: INFN Sezione di Catania and Dipartimento di Fisica e Astronomia, University of Catania, I-95123 Catania, Italy
[40] Dipartimento di Fisica, Universitá di Roma Tor Vergata, Via della Ricerca Scientifica, 1, Roma I-00133, Italy
[41] Finnish MAGIC Group: Space Physics and Astronomy Research Unit, University of Oulu, FI-90014 Oulu, Finland
[42] Japanese MAGIC Group: Institute for Space-Earth Environmental Research and Kobayashi-Maskawa Institute for the Origin of Particles and the Universe, Nagoya University, 464-6801 Nagoya, Japan
[43] INAF, Padova, Italy
[44] INFN MAGIC Group: INFN Roma Tor Vergata, I-00133 Roma, Italy
[45] Japanese MAGIC Group: Department of Physics, Konan University, Kobe, Hyogo 658-8501, Japan
[46] Department of Physics, National and Kapodistrian University of Athens, University Campus Zografos, GR 15784, Athens, Greece
[47] Institute of Accelerating Systems & Applications, University Campus Zografos, Athens, Greece
[48] Donostia International Physics Center, Paseo Manuel de Lardizabal 4, E-20118 Donostia-San Sebastián, Spain
Received 2025 September 10; revised 2025 November 5; accepted 2025 November 29; published 2026 February 2

Abstract

In 2013 April, the TeV blazar Markarian 421 underwent one of its most powerful emission outbursts recorded to date. An extensive multi-instrument campaign featuring MAGIC, VERITAS, and NuSTAR provided comprehensive very high-energy (VHE; $E > 100$ GeV) and X-ray coverage over nine consecutive days. The VHE flux peaked at approximately 15 times that of the Crab Nebula, with rapid variability detected on timescales down to 15 minutes in both X-ray and VHE bands. This rich data set, characterized by its dense temporal coverage and high photon statistics, offers an unparalleled opportunity to probe the broadband emission dynamics in blazars. In this work, we perform a detailed spectral analysis of the X-ray and VHE emissions on subhour timescales throughout the flare. We identify several clockwise spectral hysteresis loops in the X-rays, revealing a spectral evolution more complex than a simple harder-when-brighter trend. The VHE spectrum extends beyond 10 TeV, and its temporal evolution closely mirrors the behavior in the X-rays. Crucially, we report the first evidence of VHE spectral hysteresis occurring simultaneously with the X-ray loops. To interpret these findings, we apply a time-dependent leptonic model to 240 broadband spectral energy distributions (SEDs) binned on a 15 minute scale, allowing us to self-consistently track the particle distribution's history. Our modeling shows that the majority of the subhour flux and spectral variations are driven by changes in the luminosity and slope of the injected electron distribution. The required variations in the electron slope are difficult to reconcile with magnetic reconnection, but they are consistent with a shock-acceleration scenario where the shock compression ratio evolves by a factor of $\sim$2. The model also points to a relatively stable magnetic field and emitting region size, favoring a scenario where the emission originates from a stationary feature in the jet, such as a recollimation shock. However, this scenario requires a jet Lorentz factor that significantly exceeds values from VLBI measurements to account for the high minimum electron energy implied by the lack of variability in the optical band.

Unified Astronomy Thesaurus concepts: Gamma-ray astronomy (628); BL Lacertae objects (158); Non-thermal radiation sources (1119); X-ray active galactic nuclei (2035)

1. Introduction

Markarian 421 (Mrk 421; R.A. $= 11^{\rm h}4'27\overset{''}{.}31$, decl. $= 38°12'31\overset{''}{.}8$, J2000, $z = 0.031$) is the closest and among the brightest TeV blazars, which are jetted active galactic nuclei (AGNs) that have their plasma jet oriented at a small angle relative to the line of sight. Blazars are identified by a spectral energy distribution (SED) dominated by nonthermal radiation from the jet, and the SED displays two broad components. The low-energy component ranges from radio wavelengths and can reach up to the X-ray band. The high-energy component is located at gamma-ray energies. The low-energy SED component of Mrk 421 peaks above 10^{15} Hz, thus classifying it as a high synchrotron peaked blazar (HSP) following the nomenclature of A. A. Abdo et al. (2010). Thanks to its brightness, the flux evolution of Mrk 421 can be precisely characterized from radio wavelengths to very high energies (VHE; $E > 100$ GeV) by current instruments down to (at least) daily timescales, independently of the flux activity (for recent works, see, e.g., M. Baloković et al. 2016; V. A. Acciari et al. 2021; MAGIC Collaboration et al. 2021a). Because of that, Mrk 421 is an ideal target to probe blazar radiation mechanisms and investigate particle dynamics within extragalactic jets.

In 2013 April, Mrk 421 underwent one of the brightest outbursts recorded to date (V. A. Acciari et al. 2020a). The VHE flux reached $\sim$15 times that of the Crab Nebula, a factor $\gtrsim$30 above its average activity (V. A. Acciari et al. 2014). The flare lasted more than a week, and was covered over nine consecutive days by several instruments from radio bands to VHE. Notably, an extensive coverage in the X-ray and VHE regimes could be obtained thanks to the Nuclear Spectroscopic Telescope Array (NuSTAR; F. A. Harrison et al. 2013), and

[49] Corresponding authors: A. Arbet-Engels, M. Polkas, M. Petropoulou, D. Paneque (contact.magic@mpp.mpg.de).

two imaging atmospheric Cherenkov telescopes located in the Northern Hemisphere: the Major Atmospheric Gamma Imaging Cherenkov telescope (MAGIC; J. Albert et al. 2008) and the Very Energetic Radiation Imaging Telescope Array System (VERITAS; J. Holder et al. 2008). A total of 43 hr of simultaneous X-ray/VHE observation was gathered, making it one of the most extensive characterization of an HSP flare at those energies (see V. A. Acciari et al. 2020a, for details). In the context of theoretical modeling of HSP emission, the simultaneous X-ray/VHE data sample is of paramount importance since, within a leptonic emission scenario, the same electron population radiating in the X-ray band via synchrotron radiation is expected to emit in the VHE band via inverse Compton scattering (see, for example, L. Maraschi et al. 1992; A. A. Abdo et al. 2011). The obtained data sample thus provides an ideal opportunity to test and constrain theoretical models.

1.1. Summary of the 2013 April Flare and the Observed Broadband Evolution Characteristics

Initial investigations focused on the X-ray activity were reported in V. S. Paliya et al. (2015) and B. Kapanadze et al. (2016). The radio-to-VHE flux variability and correlation patterns were subsequently studied in detail in V. A. Acciari et al. (2020a, hereafter Paper I). We summarize below the main results before describing the scope of this work, which extends the study performed in Paper I.

Owing to the exceptionally high emission state, the fluxes throughout the 2013 April flare could be determined in 15 minute time bins in both the X-ray and VHE bands. Extreme variability was measured, and the light curves displayed an overall variation amplitude of more than 1 order of magnitude. In particular, significant variability down to subhour timescale was detected. Interestingly, for several of the days, the X-ray and VHE light curves could be decomposed into a slow (multihour) and fast (subhour) component, hinting toward several emitting regions contributing to those bands.

The X-ray and VHE correlation was quantified after splitting the fluxes into multiple subenergy bands: 3–7 keV, 7–30 keV, and 30–80 keV for the X-rays, and 0.2–0.4 TeV, 0.4–0.8 TeV, and >0.8 TeV for the VHE. For each combination, the VHE emission correlated strongly with the X-ray one without any time lag. However, the slope of the correlation was dependent on the exact energy bands considered. A linear relationship (slope ≈1 in a log–log flux plane) was found between the >0.8 TeV and 3–7 keV bands, while a sublinear trend (slope ≈0.4 in a log–log flux plane) was detected between 0.2–0.4 TeV and 30–80 keV bands. This complexity in the correlation patterns is in line with leptonic models (K. Katarzyński et al. 2005).

In the optical/UV and radio bands, the variability is much more suppressed compared to the VHE and X-ray regimes. The fluxes varied by at most 30%, and the corresponding flux level remained close to those measured in 2013 January–March, when Mrk 421 was exhibiting very low VHE and X-ray activity (M. Baloković et al. 2016). As for the MeV–GeV band, the flux variations were only by factors of a few. No correlation between the MeV–GeV band and the keV and TeV bands was found.

1.2. Scope of This Work

As follow-up study after Paper I, we first present an investigation of the X-ray and VHE spectral behavior. While Paper I focused on the integrated flux variability, the sensitivity of NuSTAR and MAGIC, coupled with the large photon statistics due to the high flux, offers the possibility to characterize spectral changes on subhour timescale and probe a higher degree of complexity than the common "harder-when-brighter" trend. An example of such complex spectral evolution is the so-called hysteresis pattern, which has been already measured in the X-rays, but not at VHE, likely due to a lack of statistics (M. Ravasio et al. 2004; A. U. Abeysekara et al. 2017). Hysteresis patterns provide important clues regarding the dynamics of the underlying emitting particles, since they relate to cooling losses or acceleration processes (J. G. Kirk et al. 1998).

In a second step, we build a time-dependent radiation model to describe the broadband evolution during the flare. Our work focuses primarily on the reproduction of the VHE and X-ray (flux and spectral) behavior, where the most pronounced variability happened. We applied and compared the model to multiband light curves and broadband spectra obtained over 15 minute bins. Unlike most of the previous published work that uses *time-independent* models (i.e., where particles are *not* evolved with time taking into account self-consistently radiative losses and/or escape; see, e.g., A. U. Abeysekara et al. 2017; H. E. S. S. Collaboration et al. 2020; MAGIC Collaboration et al. 2020, 2021b), our aim is to make an essential step forward to test radiation and acceleration models. We take advantage of the densely sampled VHE and X-ray observations from MAGIC, VERITAS, and NuSTAR, to constrain the evolution of the particle distribution up to the highest energies in the jet, which can then be compared with predictions from particle-in-cell (PIC) simulations.

The paper is structured as follows. In Section 2, we summarize the observations together with the data processing methods. The results of the spectral analysis are presented in Section 3. The time-dependent modeling is shown in Section 4. The discussion of our findings is given in Section 5, while our final concluding remarks are provided in Section 6.

2. Observations and Data Processing

The instruments involved in this work are the ones described in Paper I, and they cover the entire electromagnetic spectrum from radio wavelengths to VHE. As in Paper I, we consider the time period from MJD 56393 (2013 April 11) until MJD 56401 (2013 April 19). In Appendix A, the data processing is summarized. The methods are similar to those of Paper I, with the only difference being that we reprocessed NuSTAR and Fermi-LAT data with updated instrument response functions. In the VHE band, we extended the MAGIC analysis to extract spectral parameters and SED points. To extend and maximize the temporal coverage at VHE, we also make use of the VERITAS data published in W. Benbow & VERITAS Collaboration (2017), which was also used in Paper I. The multiwavelength light curves can be found in Figure 17 in Appendix A.

3. X-Ray and VHE Spectral Behaviors

We investigate the X-ray spectral evolution by fitting the NuSTAR spectra with a log-parabola model (pivot energy

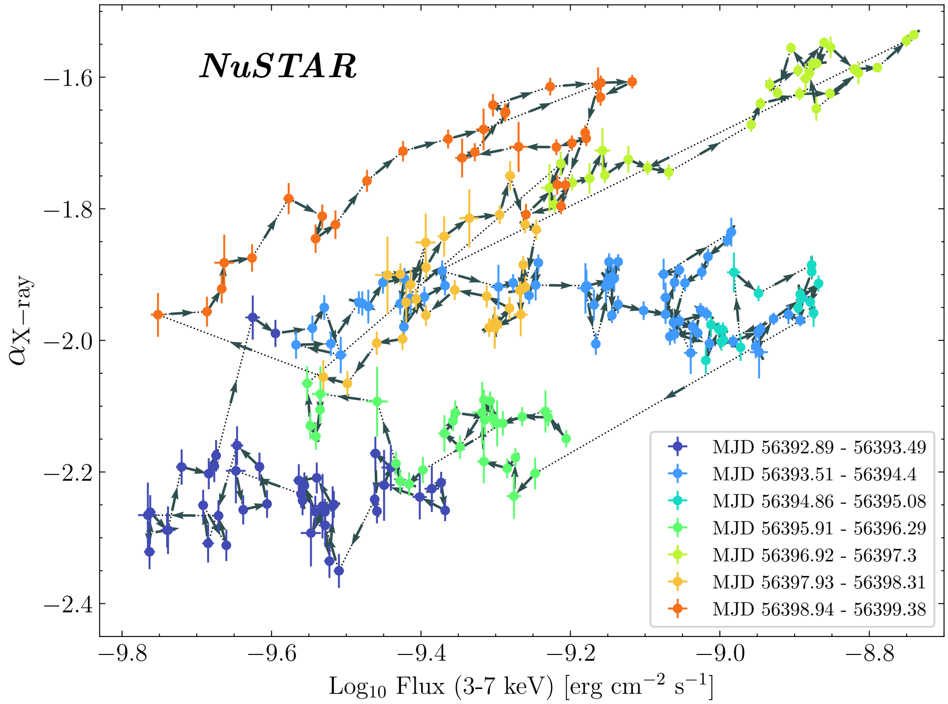

Figure 1. Spectral parameter α versus the 3–7 keV flux as measured by NuSTAR between MJD 56393 and MJD 56399. $\alpha_{\text{X-ray}}$ is derived from a log-parabola fit with the curvature parameter $\beta_{\text{X-ray}}$ fixed to 0.38 (see text in Section 2 for more details). The data are binned in 15 minute time intervals. Each day is plotted with a different color, and black arrows indicate the direction of time.

fixed at 1 keV) in the 3–79 keV band in each of the 15 minute time intervals (286 in total) of the light curve shown in Figure 17. Compared to a simple power-law model, about 60% of the bins show a $>3\sigma$ preference for a log-parabola, and therefore the latter model will be used throughout this work to characterize the spectral trends in the X-rays. After this first series of fits, we find that the curvature parameter $\beta_{\text{X-ray}}$ does not exhibit a strong dependence on the flux. The relation between $\beta_{\text{X-ray}}$ and the 3–7 keV flux is shown in Figure 18 in Appendix B. We thus perform a second series of fits in `Xspec` with $\beta_{\text{X-ray}}$ fixed to 0.38, which is the average of all the 15 minute intervals. This procedure cancels any potential correlation between the $\alpha_{\text{X-ray}}$ and $\beta_{\text{X-ray}}$ spectral parameters, and the parameter $\alpha_{\text{X-ray}}$ can be used to directly quantify the hardness evolution. We stress that, in the "β-fixed" model, the vast majority of the fits (93%) are compatible with the data within 2σ, based on a χ^2 test. For only two fits (out of 286), the "β-fixed" model is incompatible with the data with a significance above 3σ. Hence, our conclusions on the spectral evolution are not significantly biased by fixing $\beta_{\text{X-ray}}$.

In Figure 1, $\alpha_{\text{X}-\text{ray}}$ as a function of the 3–7 keV flux is displayed between MJD 56393 until MJD 56399, which is the period where the source was in its highest emission state during the flare. Each day is plotted in a different color, and black arrows show the direction of the time evolution. Significant spectral variability occurs on ~15 minute scales, and an overall harder-when-brighter behavior is detected at a significance level above 10σ (Pearson's coefficient of 0.60 ± 0.04), in line with previous NuSTAR observations of Mrk 421 (M. Baloković et al. 2016; MAGIC Collaboration et al. 2021a) and other blazars (e.g., E. Pian et al. 1998; H. Krawczynski et al. 2004). A more complex behavior is visible, however, beyond the simple harder-when-brighter trend. The source follows different paths in the parameter space depending on the day, and on different occasions spectral hysteresis loops are visible.

The first hysteresis loop in the clockwise direction is observed from MJD 56393 to MJD 56396. The flux is initially in a decaying phase on MJD 56393 (violet points) until a local minimum is reached. The emission is rising again and shows an abrupt hardening, from $\alpha_{\text{X-ray}} \approx -2.2$ to ≈ -2.0, between MJD 56393 and MJD 56394. On MJD 56396 (green markers), the emission is decreasing and softening, thus drawing a hysteresis pattern.

Two additional hysteresis loops in clockwise direction are visible over intraday timescales on MJD 56398 (light orange markers) and MJD 56399 (orange markers). It is interesting to note that the emission on MJD 56399 is significantly harder than on the rest of the days, despite covering a comparable flux range.

For the last two days discussed in this work, MJD 56400 and MJD 56401 (see Figure 17), the flux is significantly lower and $\alpha_{\text{X-ray}}$ lies between ≈ -2.2 and ≈ -2.4. For visibility purposes, these two days are not included in Figure 1, in order to focus on the MJD 56393–MJD 56399 period where most of the complex patterns are measured. They are nevertheless presented (together with the rest of the flare) in Figure 19 in Appendix B.

We performed a spectral analysis in the VHE band using the MAGIC observations. Instead of using 15 minute time intervals, as done for NuSTAR, we fit the MAGIC spectra in 30 minute intervals to increase the photon statistics, which is necessary, given the sensitivity of MAGIC. The vast majority of the MAGIC spectra are well described with the log-parabola model given in Equation (A1), and the fit p-values are all above 10^{-2}. As in the X-ray band, we find that the curvature parameter β_{VHE} shows no strong dependence on the flux. The lack of correlation between β_{VHE} and the flux above 400 GeV

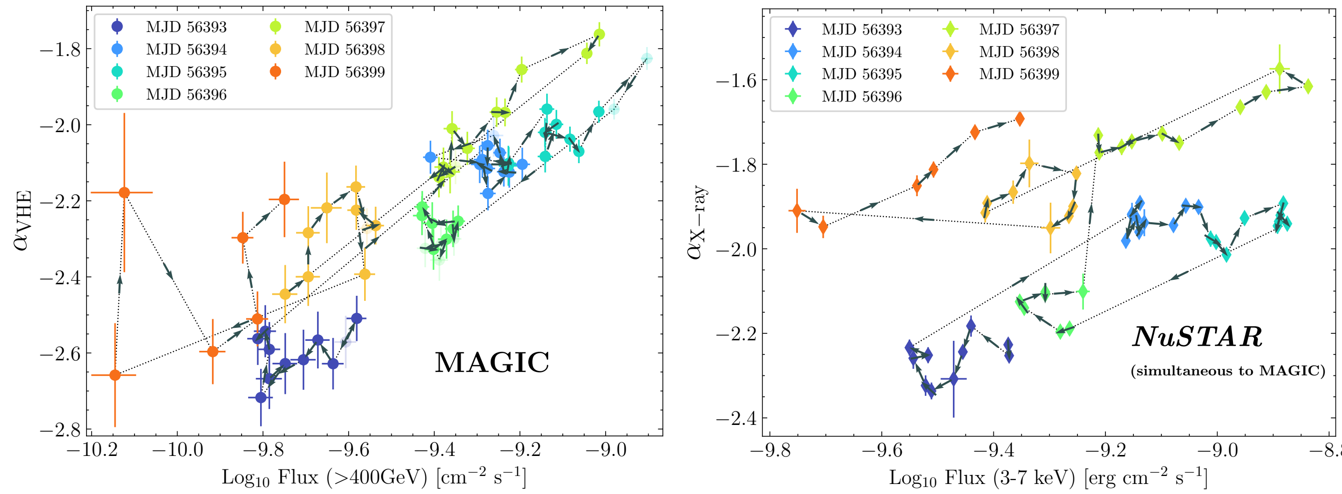

(a) (b)

Figure 2. Spectral parameter α versus flux for (a) MAGIC and (b) NuSTAR between MJD 56393 and MJD 56399. The NuSTAR fluxes are evaluated in the 3–7 keV bands, while for MAGIC they are computed above 400 GeV. In each panel, the data are binned over 30 minute, strictly simultaneous intervals. Each day is plotted with a different color, and black arrows indicate the direction of time. The MAGIC points plotted with transparent markers are temporal bins that are not accompanied by a strictly simultaneous NuSTAR measurement.

is shown in Figure 18 in Appendix B. Given this lack of correlation, and for the same arguments mentioned previously in the case of the NuSTAR spectral analysis, a second series of fits were performed with $\beta_{\rm VHE}$ fixed to 0.40 (the average from all the individual time intervals). We also note that, based on a χ^2 test, the "β-fixed" model is consistent with the data within 3σ for all fits (73 in total), and only two fits are inconsistent with the data above 2σ. No significant bias is thus introduced in our interpretation of the spectral evolution when using a "β-fixed" model. Finally, we ran all fits above a common minimum energy of 250 GeV, such that $\alpha_{\rm VHE}$ can be fairly compared between all time intervals. The energy threshold of MAGIC increases with the observing zenith angle, and using a threshold at 250 GeV instead of the minimum achievable by MAGIC ($\sim$75 GeV) allows us to include time bins with an observing zenith angle up to $\approx 52^\circ$ while preserving sufficient statistics. Only a minority of the bins were taken at zenith angles above 52°, and they are removed from the spectral analysis.

In Figure 2(a), we show $\alpha_{\rm VHE}$ as function of the flux above 400 GeV. For comparison purposes, in Figure 2(b), the spectral index $\alpha_{\rm X\text{-}ray}$ is plotted as function of the 3–7 keV flux based on 30 minute time intervals strictly simultaneous with those of MAGIC. Overall, the MAGIC spectra reveal a significant harder-when-brighter trend at VHE. This is in agreement with previous work on Mrk 421 (e.g., V. A. Acciari et al. 2021; MAGIC Collaboration et al. 2021a). The correlation significance is $\approx 11\sigma$ and the Pearson coefficient is 0.86 $\pm$ 0.03. The significance is mostly dominated by the day-by-day variations; however, we note a significant ($\gtrsim 5\sigma$) intranight harder-when-brighter behavior measured on MJD 56397.

Similar to what was observed in the hard X-rays, the VHE spectra populate different regions in the parameter space depending on time. Figure 2 unveils an evident similarity between the behavior observed in MAGIC and NuSTAR, and $\alpha_{\rm VHE}$ and $\alpha_{\rm X\text{-}ray}$ draw similar patterns in the parameter space throughout the entire flare. On MJD 56398 (orange data points), the evolution of $\alpha_{\rm VHE}$ strongly indicates an intraday hysteresis loop in the clockwise direction, simultaneous with the one observed in NuSTAR.

3.1. Daily VHE Spectral Analysis

In this section, we investigate the nightly averaged MAGIC spectra, which will be used as input for the time-dependent modeling of the flare to constrain parameters such as the Doppler factor or the magnetic field within the source. In a leptonic scenario, the highest energies (above a few TeVs) are affected by the Klein–Nishina suppression of the inverse Compton cross section. Averaging VHE spectra on each night provides a precise characterization of the multi-TeV spectrum, allowing us to probe the presence (or absence) of a cutoff.

For most of the days, the nightly MAGIC spectra show a $>3\sigma$ statistical preference for a log-parabola model with an exponential cutoff (dubbed the ELP) instead of a pure log-parabola model (as applied to the 30 minute intervals; see previous section). We parameterize the ELP as follows:

$$\frac{dN}{dE} = f_0 \left(\frac{E}{E_0}\right)^{\alpha - \beta \log_{10}\left(\frac{E}{E_0}\right)} e^{-\frac{E}{E_{\rm cut-off}}}, \qquad (1)$$

where E_0 is the normalization energy fixed to 500 GeV. The best-fit parameters are listed in Table 1, together with the χ^2/d.o.f. and the statistical preference for an ELP model ($\sigma_{\rm ELP}$). For days MJD 56398 to MJD 56401, the preference for an ELP model is not significant ($<3\sigma$); thus, we only quote the parameters of the best-fit log-parabola function. The measured spectra extend to $\sim$10 TeV, at which the EBL absorption becomes significant for Mrk 421 ($\tau_{\rm EBL} \sim 1$). We thus tried different available EBL models (A. Franceschini et al. 2008; R. C. Gilmore et al. 2012; A. Franceschini & G. Rodighiero 2018) to search for possible systematic effects, but all results were compatible with fits using the A. Domínguez et al. (2011) model.

Days MJD 56395 and MJD 56397 are characterized by the hardest spectra and the highest cutoff energies, located at $\sim$5 TeV and $\sim$13 TeV for MJD 56395 and MJD 56397,

Table 1
Spectral Parameters Obtained by Fitting the Nightly Averaged MAGIC Spectra

Date MJD	f_0 (TeV cm^{-2} s^{-1})	$\alpha_{\rm VHE}$	$\beta_{\rm VHE}$	$E_{\rm cutoff}$ TeV	χ^2/d.o.f.	$\sigma_{\rm ELP}$
56393	$(0.69 \pm 0.05) \times 10^{-9}$	-2.36 ± 0.09	0.31 ± 0.08	2.8 ± 1.1	17.0/14	3.0
56394	$(1.49 \pm 0.04) \times 10^{-9}$	-1.92 ± 0.04	0.03 ± 0.04	2.9 ± 0.4	15.0/16	8.6
56395	$(2.21 \pm 0.03) \times 10^{-9}$	-1.83 ± 0.02	0.14 ± 0.03	4.7 ± 0.7	7.8/16	7.7
56396	$(1.27 \pm 0.05) \times 10^{-9}$	-2.06 ± 0.05	0.14 ± 0.05	2.7 ± 0.5	14.5/15	6.4
56397	$(1.34 \pm 0.01) \times 10^{-9}$	-1.91 ± 0.02	0.12 ± 0.03	13 ± 4	22.3/16	3.2
56398	$(0.65 \pm 0.01) \times 10^{-9}$	-2.30 ± 0.01	0.36 ± 0.02	⋯	13.7/16	2.1
56399	$(0.38 \pm 0.01) \times 10^{-9}$	-2.34 ± 0.03	0.40 ± 0.05	⋯	23.9/15	0.0
56400	$(0.30 \pm 0.01) \times 10^{-9}$	-2.58 ± 0.04	0.69 ± 0.10	⋯	19.5/15	1.8
56401	$(0.15 \pm 0.01) \times 10^{-9}$	-2.96 ± 0.12	0.96 ± 0.39	⋯	10.5/12	0.0

Note. An ELP model (see Equation (1)) is fitted for days MJD 56393 to MJD 56397. For days MJD 56398 to MJD 56401, a simple log-parabola model is adopted, since the statistical preference for an ELP is $<3\sigma$. The statistical preference for an ELP is given in the last column.

respectively. The spectra from these two nights are overlaid in Figure 3, where we compare a log-parabola fit (dotted lines) with an ELP model (dashed lines). For MJD 56397, we set the lower limit on $E_{\rm cutoff}$ at the 95% confidence level (C.L.) by performing a χ^2 scan around the best-fit $E_{\rm cutoff}$. During the scan, all parameters are left free except $E_{\rm cutoff}$. The 95% C.L. limit is given by the $E_{\rm cutoff}$ value at which the χ^2 increases by 2.71 with respect to the minimum ($\chi^2_{\rm min}$). Following this procedure, the 95% C.L. lower limit on $E_{\rm cutoff}$ is 8.3 TeV.

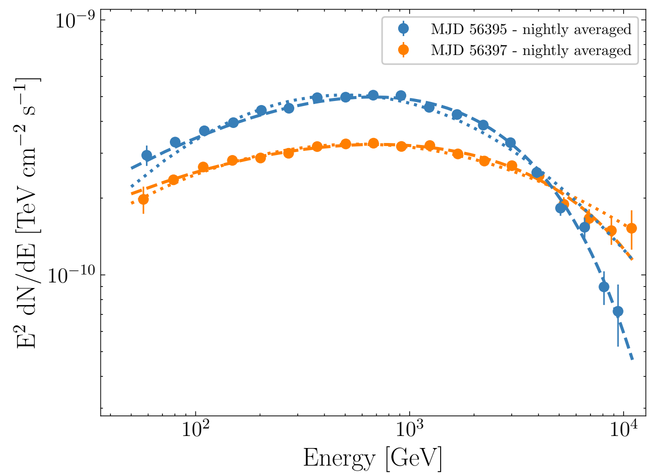

Figure 3. Nightly MAGIC spectra from MJD 56395 and MJD 56397, which show the highest VHE flux of the 2013 April flare. The dotted and dashed lines are the best-fit function using a log-parabola and a log-parabola with a cutoff model, respectively. For both days, the log-parabola model with a cutoff is preferred at a significance level above 3σ. The SED points and spectral model curves are corrected for the EBL absorption using the model of A. Domínguez et al. (2011).

4. Time-dependent Modeling of the Flare

Our time-dependent model assumes a purely leptonic scenario for the nonthermal emission. The optical-to-X-ray fluxes originate from synchrotron radiation by relativistic electrons/positrons within the jet (hereafter, for simplicity, both particle types are denoted as "electrons"), while the gamma-ray flux is produced via electron inverse Compton scattering off the synchrotron photons emitted by the same population of electrons. This model is commonly referred to as the synchrotron self-Compton model (SSC; see, for example, L. Maraschi et al. 1992; F. Tavecchio et al. 1998; H. Krawczynski et al. 2004), and is usually able to reproduce well the SED of Mrk 421 (see, e.g., A. A. Abdo et al. 2011; A. U. Abeysekara et al. 2017; MAGIC Collaboration et al. 2021a). The SSC scenario is supported by the tight correlation between the X-ray and VHE fluxes (see results in Paper I), and the similar simultaneous spectral evolution patterns in those bands (see Section 2). This strongly indicates a single underlying particle population responsible for the two SED components (here, the electrons), thus differing from hadronic models (K. Mannheim 1993; A. Mücke & R. J. Protheroe 2001) that additionally invoke protons to explain the gamma-ray emission.

The model consists of two spatially separated, noninteracting emitting regions inside the jet. The first zone, more compact and energetic, dominates the emission in the X-ray and VHE bands. The second zone occupies a larger volume and is populated with less energetic electrons such that it is dominantly responsible for radio-to-optical and MeV/GeV emission. At radio frequencies, the fluxes are treated as upper limits, given that they likely receive a substantial contribution from broader regions located much farther downstream the jet. Such a multiple-component approach is suggested by the strong correlation between the X-ray and VHE bands, while the X-ray/VHE emissions do not correlate with the radio/optical/MeV–GeV fluxes. Moreover, the optical/UV fluxes vary by at most 30%, while X-ray and VHE fluxes display flux changes by about an order of magnitude (see Paper I and Figure 17).

In the first zone (hereafter dubbed as the "fast" zone), the parameters and the electron distribution are evolved on $\lesssim$15 minute timescales to account for the X-ray and VHE variability on subhour timescales (see previous sections). As for the second zone (hereafter dubbed as the "slow" zone), variations of the parameters are imposed on daily timescales because the radio/optical/MeV–GeV show no significant intranight variability. The modeling of the light curve and SEDs is performed for the nine days of the flare (see Figure 17), and solely within time ranges where strictly simultaneous X-ray and VHE measurements are available.

4.1. Model Setup and Initial Conditions

Each emitting zone is modeled as a sphere (in the jet comoving frame) of radius R permeated by a tangled magnetic field of strength B. The emitting plasma moves with a bulk velocity of Γ_b, leading to a relativistic beaming of the radiation with a Doppler factor δ. Preaccelerated electrons are injected at a rate $Q_e^{\rm inj}(\gamma)$ into each zone, with a power-law distribution of Lorentz factor γ (or equivalently, kinetic energy $(\gamma - 1)\, m_e c^2 \approx \gamma\, m_e c^2$) with a slope p between $\gamma_{\rm min}$ and $\gamma_{\rm max}$, and followed by a modified exponential cutoff for Lorentz factors beyond $\gamma_{\rm max}$:

$$Q_e^{\rm inj}(\gamma) \propto \begin{cases} \gamma^{-p}, & \gamma_{\rm min} < \gamma < \gamma_{\rm max} \\ \gamma^{-p} \exp\left(1 - (\gamma/\gamma_{\rm max})^a\right), & \gamma > \gamma_{\rm max} \end{cases}, \qquad (2)$$

where $a = 2$, which we find to yield the best description of the spectral hardness and the fluxes at all bands. In principle, within a shock acceleration process, the exponent a can be related to the type of diffusion/turbulence in the plasma (see, e.g., V. N. Zirakashvili & F. Aharonian 2007; C. Baheeja et al. 2024), and $a = 2$ may occur in a Bohm-type diffusion. Superexponential high-energy cutoffs are also derived from PIC simulations of magnetic reconnection events (see, e.g., G. R. Werner et al. 2016), although recent simulations of large-scale systems seem to prefer a simple exponential cutoff (M. Petropoulou & L. Sironi 2018). The normalization of the distribution is characterized by the electron compactness l_e. The electron compactness is a dimensionless measure of the electron luminosity L_e, and is defined as follows:

$$L_e = m_e c^2 \int_{\gamma_{\rm min}}^{\gamma_{\rm max}} Q_e^{\rm inj}(\gamma)(\gamma - 1) \qquad (3)$$

$$l_e = \frac{3\sigma_T L_e}{4\pi m_e c^3 R}. \qquad (4)$$

After injection, the subsequent electron and photon populations can be exactly determined by solving the Fokker–Planck equations (referred to as kinetic equations, hereafter), taking into account all the gain/loss terms of all relevant radiative processes. These are the emission from synchrotron and inverse Compton scattering, the synchrotron self-absorption, and the $\gamma\gamma$ pair-production. We note that, for the inverse Compton scattering in the Klein–Nishina regime, the full expression is used (G. R. Blumenthal & R. J. Gould 1970). We further assume that, in both zones, the particles escape the emitting region on a timescale $t_{\rm esc} = R/c$. When solving the kinetic equations, the Compton scattering of cold electrons ($\gamma \approx 1$) and their radiation are not considered.[50] For solving the kinetic equations, we use a modified version of the code of A. Mastichiadis & J. G. Kirk (1995), as further developed in M. Polkas et al. (2021) for producing time-dependent SEDs by continuously varying one parameter of the SSC model. The main differences with their work and the current model are as follows: (i) we use high-cadence X-ray light curves (binned over 15 minute intervals) instead of gamma-ray light curves of 1 day resolution; (ii) we impose variations on the power-law slope of the electrons p; (iii) we use l_e variations as a correction motivated by the model-data residuals following the variations of p (see later for more details); and (iv) no external photon fields are considered as seeds for the inverse Compton scattering. The general scheme for transforming from observations to model parameters and the interpolation scheme applied remains the same. In our setup, the energy resolution is fixed at 0.1 dex.

The kinetic equations for electrons and photons are solved in the rest frame of the blob. We therefore have to transform the properties of the photon field to the observer's frame using the Doppler factor δ. The bolometric luminosities transform as δ^4, the photon energies are transformed via multiplying by δ, and time contracts as $1/\delta$. The photon distribution is transformed to an observed SED, using the distance of Mrk 421 ($z = 0.031$; M. H. Ulrich et al. 1975). These transformations are not going to be mentioned again for the rest of this section.

4.1.1. Stationary States

The time-dependent modeling starts from stationary states determined for each day separately. For this, we first build daily average SEDs from the data, which we then model with our two-component scenario. We extract daily VHE spectra from the MAGIC observations as well as NuSTAR SEDs averaged over time ranges that are strictly simultaneous with those from MAGIC. The NuSTAR SEDs are complemented by Swift-XRT observations that are the closest to the center of the MAGIC/NuSTAR exposures. We also use Fermi-LAT SEDs averaged over 18 hr around the center of each MAGIC/NuSTAR observation. Finally, we consider quasi-simultaneous radio/optical/UV observations (within less than ∼10 hr, i.e., smaller than the typical variability timescale observed at those frequencies).

We compute the steady-state spectrum of each zone separately by running the code until 10 light-crossing times without applying any parameter variations and then add their SEDs. The total spectrum is compared to the data. We update the input parameters and repeat the procedure until a satisfactory description of the measurement is achieved.

In order to limit the degrees of freedom, the Doppler factor of the "slow" zone is set to $\delta_{\rm slow} = 30$ (in line with previous modeling of this source in an average state; see A. A. Abdo et al. 2011), and the electrons are injected with an index $p = 2$ for all days, which is found to describe the radio/optical/MeV–GeV data well. We constrain the radius of the emitting blob to be consistent with the variability timescale using causality arguments ($R < \delta_{\rm slow}\, c\, \Delta t_{\rm obs}$, where $\Delta t_{\rm obs}$ is the observed variability timescale, which is ∼1 day for the radio/optical/MeV–GeV bands). We find that using $B \approx 0.07$ G provides a reasonable description of the data, and hence we fix it to the latter value for all days.

Similar considerations are made to constrain the degrees of freedom for the stationary states of the "fast" zone. First, we derive that $\delta_{\rm fast} \sim 100$ is required in order to properly reproduce the VHE spectra up to the highest energies. As highlighted in Section 3.1, MAGIC nightly spectra extend over multi-TeV energies. Adopting a lower Doppler factor, $\delta_{\rm fast} \sim 50$, comparable to that of the "slow" zone, leads to an evident underestimation of the measurements at the highest energies, due to the Klein–Nishina suppression of the inverse Compton cross section. Following F. Tavecchio et al. (1998), the Klein–Nishina effects fully set in and strongly affect the peak frequency (and luminosity) of the inverse Compton component when the Doppler factor is below $\delta_{\rm KN}$, as given by

[50] The emission from electrons with $\gamma \approx 1$ is very low, so we assume that, once they cool down to such energies, they simply escape the blob. Additionally, the code used in this work is not designed to treat both nonrelativistic and relativistic particle distributions.

the following:

$$\delta_{\rm KN} = \sqrt{\frac{\nu_{\rm s}\nu_{\rm IC}}{(3/4)(m_e c^2/h)^2}}, \quad (5)$$

where $\nu_{\rm s}$ and $\nu_{\rm IC}$ are the observed synchrotron and inverse Compton peak frequencies, respectively, and h is the Planck constant. Taking MJD 56395 as an example, we have $\nu_{\rm s} \approx 1$ keV and $\nu_{\rm C} \approx 1$ TeV (see Figure 3), yielding $\delta_{\rm KN} \approx 70$. We stress that, even above this limit, the Klein–Nishina effects can have a non-negligible impact, and we find that increasing the Doppler factor to at least $\delta_{\rm fast} \sim 100$ is necessary to obtain a satisfactory description of the VHE data up to the highest energies for most days. In Appendix C, we compare, for illustration purposes, the SED from the "fast" zone when $\delta_{\rm fast} = 50$ and $\delta_{\rm fast} = 100$ for MJD 56393 and MJD 56395. These tests confirm the expected underestimation of the VHE spectrum at the highest energies when a Doppler factor below 100 is used. As reported in detail in Section 4.2, MJD 56397 still suffers from an underprediction of the highest VHE spectral points, even when using $\delta_{\rm fast} = 100$. While we argue that it may also suggest the appearance of an extra zone filled with energetic electrons, one cannot exclude that, for this particular day, the Doppler could be even larger than 100.

The radius of the "fast" zone is set to $R = 0.122 \times 10^{16}$ cm, in agreement with the ∼15 minute variability detected in the X-ray and VHE bands. In contrast to the "slow" zone, the magnetic field is kept as a free parameter, which is a requirement to match the variation of the Compton dominance (ratio between the inverse Compton and synchrotron peak luminosities) that is well-constrained by the X-ray and VHE data. Finally, the injected electron slope (p) is determined directly from the X-ray data.

The model curves for these stationary states, adjusted to the daily broadband SEDs, are depicted in Figure 4 and 5. The corresponding model parameters are listed in Table 2, and their temporal evolution is illustrated in Figure 6. Within the "fast" zone, the magnetic field B varies by less than a factor of two. Regarding the "slow" zone, most of the parameters remain unchanged, in line with the low variability observed in the UV/optical/MeV–GeV fluxes.

The small variability of R and B throughout the days suggests that both components are almost stationary within the jet. In case the "fast" zone moves downstream (as in a blob-in-jet model) with a Lorentz factor $\Gamma_{\rm b,fast} \sim \delta_{\rm fast}/2 = 50$ (assuming a closely aligned jet), one can estimate a traveled distance of $\Delta d = \frac{\Gamma^2_{\rm b,fast}\beta_{\rm fast} c \Delta T_{\rm obs}}{1+z} \sim 10^{20}$ cm ∼30 pc within a window of $\Delta T_{\rm obs} = 9$ days in the observer's frame. Assuming that the blob started to form at a distance $d_0 \sim R/\Theta_d \sim R\,\Gamma_{\rm b,fast} \sim 10^{17}$ cm from the jet's base (where $\Theta_d \sim 1/\Gamma_{\rm b,fast}$ is the opening angle of the jet), this leads to a ratio $\Delta d/d_0 \sim 10^3$. Under the assumption where the magnetic field scales as $\sim R^{-1}$ (due to flux freezing and energy conservation in a toroidal field; M. C. Begelman et al. 1984), B would evolve by several orders of magnitude between the start and the end of the flare, in clear contradiction with Table 2. We thus favor a scenario where the two zones are quasi-stationary features in the jet, possibly associated with two different recollimation shocks (R. A. Daly & A. P. Marscher 1988). In this configuration, even considering stationary shocks, the radiation is boosted by a factor δ^4 (see discussion in M. Sikora et al. 1997; A. Zech & M. Lemoine 2021).

We neglect the interaction between the two regions, meaning that the emission from each zone is entirely computed based on the local physical conditions. In reality, particles in a given zone may interact with the radiation field from the other zone if these are close to each other, leading to an additional inverse Compton component. In our case, the interaction is enhanced by the relative bulk velocity of the plasma of the zones that inevitably boosts the radiation density of each zone as seen in the frame of the other. Based on the parameters of Table 2, we estimate that if the two zones (possibly recollimation shocks) are separated along the jet's axis by at least $r_0 > 1.5 \times 10^{17}$ cm, the interaction can be safely neglected. Such a separation, equivalent to $\lesssim 10^{-1}$ pc, is realistic and well below the scale of the jet and the distance between the stationary features detected in Mrk 421 (M. L. Lister et al. 2016; O. Hervet et al. 2019). The detailed quantification is presented in Appendix D.

The parameters for the "slow" zone are only evolved on a daily timescale according to Table 2. This is in line with the variability noticed in the radio/optical/MeV–GeV bands (Figure 17). On the other hand, the rapid X-ray and VHE spectral changes imply intranight variations of the parameters in the "fast" zone. We try to reproduce the X-ray and VHE data by evolving p and l_e. The variations are applied on timescales equal to the light-crossing time, which is $R/c/\delta_{\rm fast} \sim 6$ minutes in the observer's frame. The procedure is described below.

4.1.2. Time-dependent Intraday SED Modeling

For each day, the p and l_e variations in the "fast" zone are applied with all other model parameters fixed to the values of Table 2. We build time evolution curves of p and l_e in the observer's frame, which are then transformed in the jet's rest frame by multiplying by $\delta_{\rm fast}$, and then are smoothed with a quadratic interpolation so that the derivatives are handled correctly when solving the stiff kinetic equations. We reiterate that the code outputs model curves with temporal steps equal to the light-crossing time, which is $R/c/\delta_{\rm fast} \sim 6$ minutes in the observer's frame. To remove potential artifacts originating from the initial conditions, we let the system reach a steady state (by evolving the system for 0.1 days, equivalent to ≈25 light-crossing times) before we start applying the variations in model parameters.

We follow a two-step approach when applying the simultaneous p and l_e variations. We start by building light curves by varying only p. To determine the time series of p, we directly exploit the X-ray data (using Swift-XRT and NuSTAR), as this energy regime of the SED originates from synchrotron radiation, whose spectrum brings a direct constraint on the electron slope at any time throughout the flare. The details on the determination of the p are provided in Appendix E. In summary, we approximate the NuSTAR data with a simple power-law model, which is used to estimate the photon index $\Gamma_{\rm X-ray}$ in the soft X-ray band that is radiated by electrons far below the high-energy (exponential) cutoff. The slope p of the injected electrons is then derived using the relation $\Gamma_{\rm X\text{-}ray} = (p+1)/2$ for a synchrotron-uncooled population of electrons (G. B. Rybicki & A. P. Lightman 1979), which is the case for all stationary states derived in the previous section. In fact, by balancing the escape timescale, R/c, with the synchrotron and inverse Compton

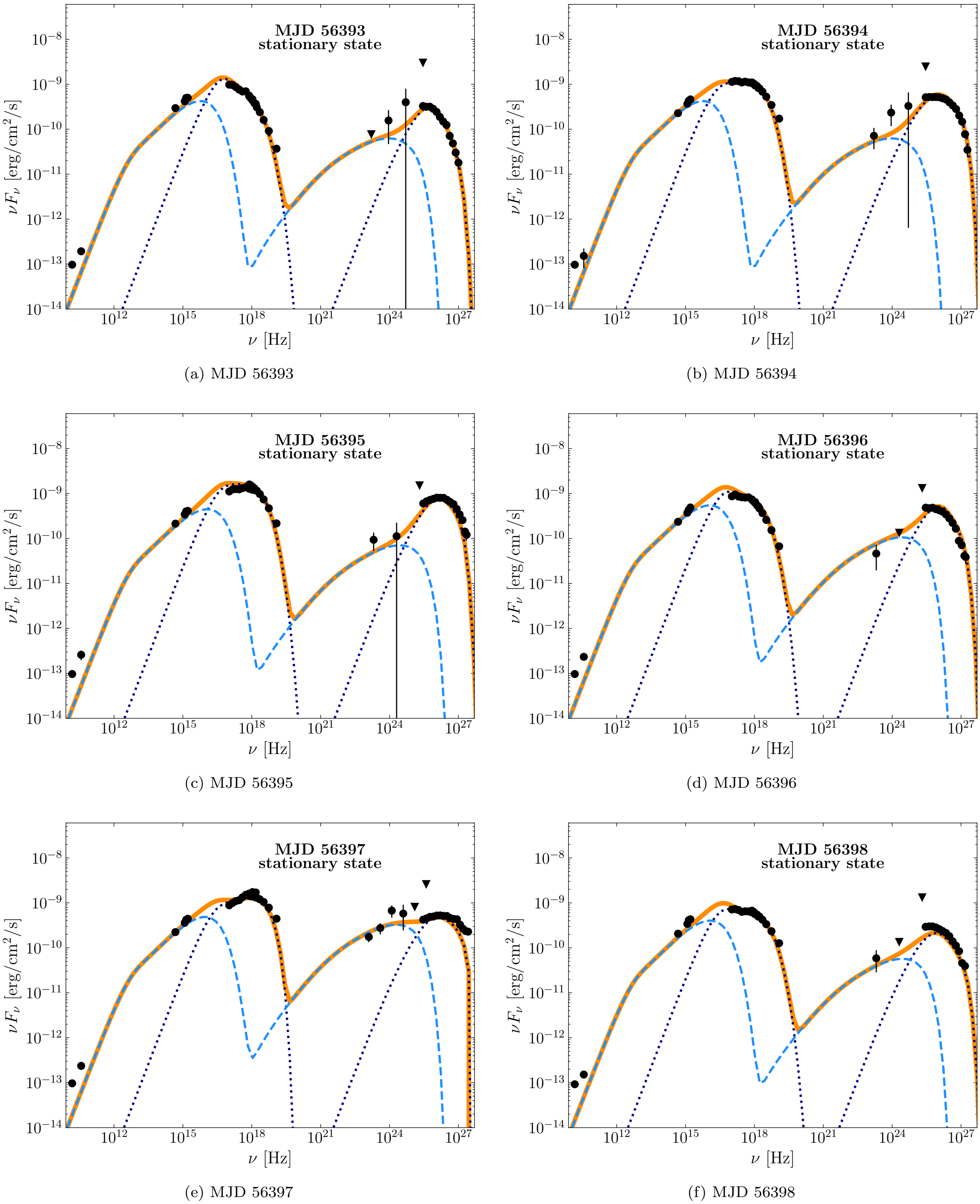

Figure 4. Stationary states fitted to nightly averaged SEDs, from MJD 56393 to 56398. The light blue dashed line represents the emission from the "slow" zone, the dark blue dotted line is the emission from the "fast" zone, and the solid line is the sum of the two components. Data are depicted with dark points. The corresponding model parameters are listed in Table 2.

cooling timescales, the cooling break is located around $\log_{10}\gamma \sim 6.2$, beyond the cutoff Lorentz factor γ_{max} of the injected distribution.

After running the code with the p variations, the X-ray and VHE flux from the model differ significantly from that of the data, since the observed variations are significantly more

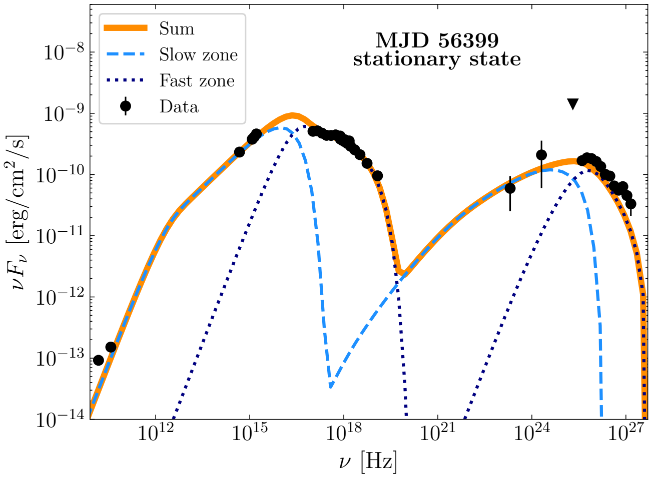

(g) MJD 56399

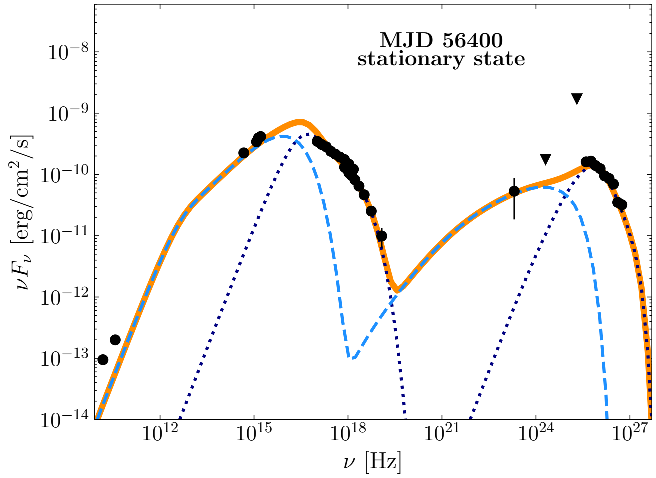

(h) MJD 56400

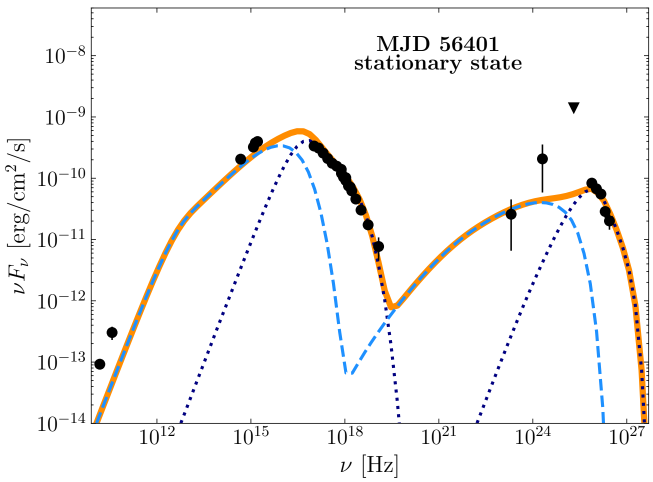

(i) MJD 56401

Figure 5. Same as Figure 4, from MJD 56399 to MJD 56401.

intense than those generated with a p-only evolution in the electron population. That is expected, given the observed multiband amplitude of variations. For the aforementioned reasons, we correct for the unaccounted flux variations by directly evolving l_e. To do so, we need to know at each time t what is the amount of flux to be added/subtracted, as well as how to translate this flux difference to an electron compactness difference. As in M. Polkas et al. (2021), we assume a power-law dependence of l_e on the flux of a certain band, and we select here the 3–7 keV 15 minute light curve from NuSTAR as our reference band:

$$l_e(t) = l_{e,0} \times \left(\frac{F_{3-7\mathrm{keV}}(t)}{F_{3-7\mathrm{keV},0}}\right)^{1/\sigma_x}. \tag{6}$$

We find that the value $\sigma_x \approx 1$ yields a good description for all days. Note that, for the SSC scenario, the compactness of synchrotron (here also X-ray) photons $l_{\rm syn}$ is expected to have a linear/square-root dependence on l_e in the slow/fast synchrotron-dominated/fast SSC-dominated cooling regime (Equation (A7) in M. Polkas et al. 2021). However, this does not take into account the dependence of $F_{3-7\mathrm{keV}}(t)$ on the spectrum of the photon distribution (which also changes with varying electron compactness) when close to transiting cooling regimes. We compute the residuals $\Delta F = F_{3-7\mathrm{keV,data}}–F_{3-7\mathrm{keV,p}}$, where $F_{3-7\mathrm{keV,p}}$ stands for the flux for the p-variation simulation. Then, for each point, we create a synthetic l_e time curve as $l_e(t) = l_{e,0} \times (1 + \Delta F/F_{3-7\mathrm{keV,p}})^{1/\sigma_x}$, where $l_{e,0}$ is the value determined from the stationary state. We then apply this time series, together (values are changed at the same substep in the code) with the initial p light curve on the blob that has reached the quasi-steady state, and produce the final time-dependent electron and photon distributions. The SED of the "slow" zone (transformed with $\delta_{\rm slow} = 30$) is added to the contribution of the "fast" zone using the parameters given in Table 2 in order to obtain the broadband emission at each time.

The simultaneous evolution of the injected p and l_e in the "fast" zone at each time step is presented in Figure 7. The model is applied over time intervals with NuSTAR and VHE exposures. For illustrative purposes, we also plot in Figure 8 snapshots of the resulting electron distribution at a fixed time for each day (we arbitrarily select the start of the day in MJD units). To give an idea of the intraday variations of the electron distribution, Figure 9 presents with bands the range of values covered during three different days.

Table 2
Stationary State Model Parameters for Each Day for the "Slow" and "Fast" Zones (δ_{slow} = 30 and δ_{fast} = 100, Respectively)

Day	$\log_{10}(l_e) + 5$	p	$\log_{10}(\gamma_{min})$	$\log_{10}(\gamma_{max})$	B (G)	R (10^{16} cm)
"Slow" zone				$\delta = 30$		
56393	0.10	2.0	2.5	4.4	0.21	1
56394	0.10	2.0	2.5	4.4	0.21	1
56395	0.20	2.0	2.5	4.6	0.21	1
56396	0.10	2.0	2.5	4.6	0.21	1
56397	0.70	2.0	2.5	4.5	0.21	0.5
56398	0.00	2.0	2.5	4.6	0.21	1
56399	0.15	2.0	2.5	4.5	0.21	1
56400	−0.05	2.0	2.5	4.5	0.21	1
56401	0.05	2.0	2.5	4.5	0.21	1
"Fast" zone				$\delta = 100$		
56393	−0.30	3.63	4.2	5.2	0.160	0.122
56394	−0.10	2.94	4.3	5.3	0.100	0.122
56395	−0.05	2.82	4.3	5.3	0.110	0.122
56396	−0.10	3.20	4.3	5.3	0.100	0.122
56397	−0.10	2.61	4.2	5.4	0.100	0.122
56398	−0.30	3.11	4.2	5.4	0.120	0.122
56399	−0.45	3.35	4.2	5.5	0.130	0.122
56400	−0.30	3.96	4.3	5.4	0.086	0.122
56401	−0.55	3.96	4.3	5.3	0.110	0.122

Note. The day labeling refers to the MJD date entering during this segment. The values of p for the "fast" zone are representative of the daily average state, and additional short-timescale variations will be applied to model the light curves (see Section 4.1.2 and Figure 7).

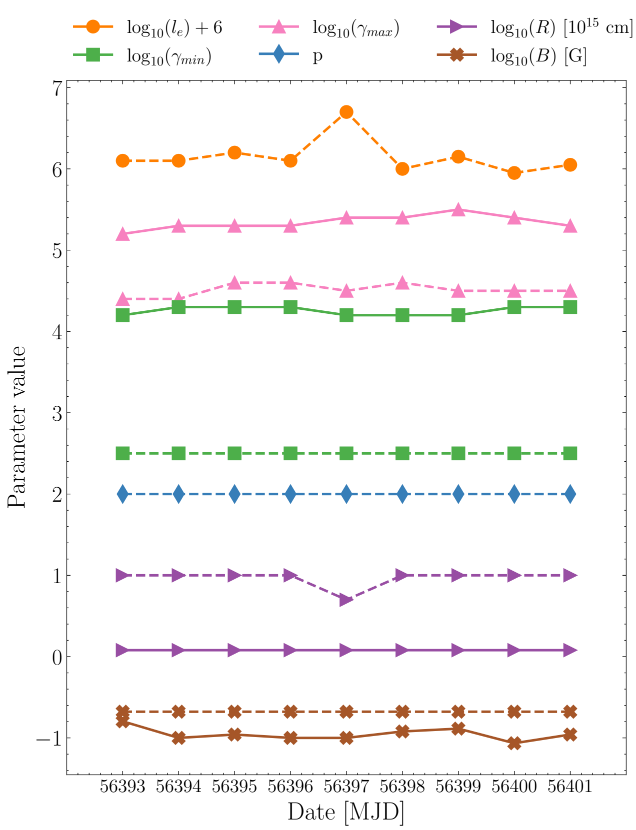

Figure 6. Temporal evolution of the parameters from the theoretical model applied to broadband SEDs from single days. The solid and dashed lines depict the model parameters from the "fast" and "slow" zones, respectively.

4.2. Multiband Light Curves from the Theoretical Model and Comparison to the Measurements

The optical and MeV–GeV emissions, which display small and slow variations, are reproduced well by the "slow" component, as shown in Figures 4 and 5. Therefore, this section focuses on the data/model comparisons of the light curves in the X-ray and VHE bands, which are dominated by the model parameters related to the "fast" component.

From the broadband SEDs derived by our time-dependent theoretical model, we compute fluxes in the 3–7 keV, 7–30 keV, 30–80 keV, 0.2–0.4 TeV, 0.4–0.8 TeV, and >0.8 TeV bands, which are the same energy ranges used in the analyses of the observational data from NuSTAR and MAGIC/VERITAS. The fluxes are extracted by fitting a log-parabola function to the model SED curves (with a curvature β left as a free parameter). The best-fit function is then integrated in each energy band to extract the flux in units of 1 $cm^{-2}\,s^{-1}$ for the VHE, and erg $cm^{-2}\,s^{-1}$ for the X-rays. The VHE photon fluxes are extracted after including EBL absorption using the model of A. Domínguez et al. (2011), which is the same template used throughout this work, as well as for the MAGIC spectral analysis (Section 3). Finally, we average the model fluxes over 15 minute temporal bins, as done for the data (the code provides model curves in temporal steps of ~6 minutes in the observer's frame).

The results are presented in Figures 10 and 11 for the X-ray and VHE bands, respectively. The residuals, defined as $\frac{(\text{data} - \text{model})}{\text{model}}$, are given on the bottom panel of each light curve. Histograms of the residuals can be found in Figures 12 and 13.

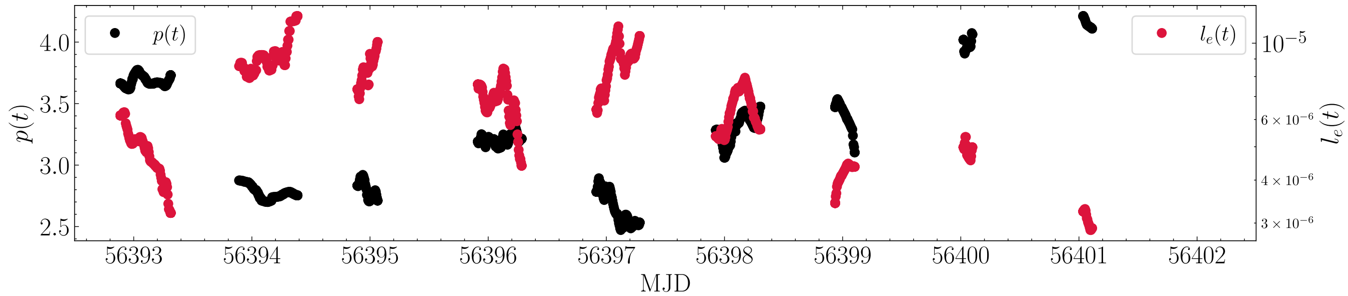

Figure 7. Temporal evolution of the model parameters $p(t)$ (black markers) and $l_e(t)$ (red markers) that characterize the electron distribution injected in the "fast" zone. See text for more details on the procedure applied to determine the corresponding variations.

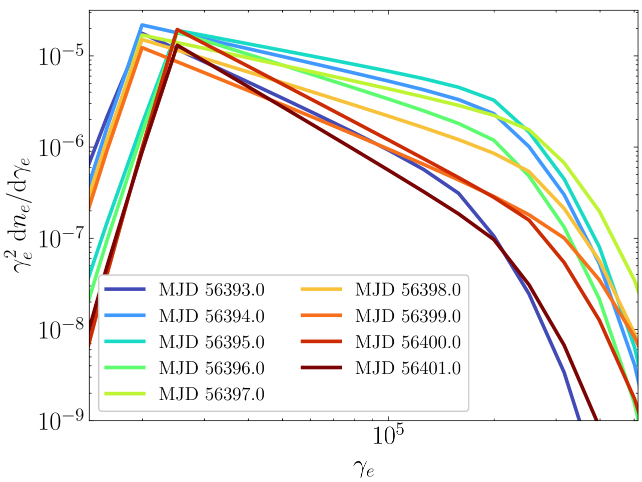

Figure 8. Snapshots from the temporal evolution of the electron distribution in the "fast" zone, extracted at the time MJD 56XXX.0 from each day of the flare. Here, n_e is defined as the number of particles contained in a volume $\sigma_T R$.

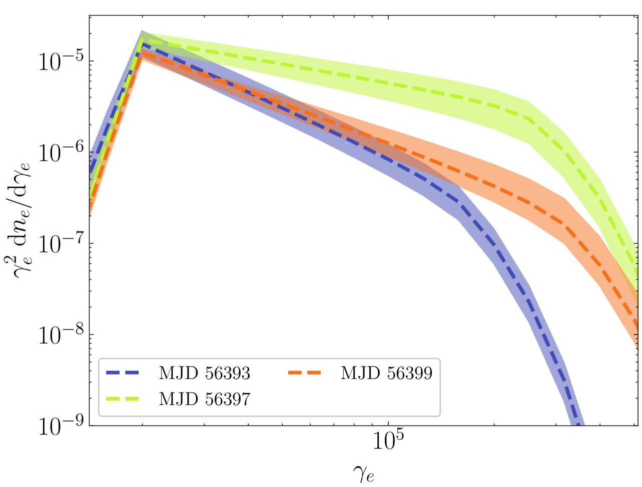

Figure 9. Range of values covered by the electron distributions from three selected days that relate to the beginning (MJD 56393), middle (MJD 56397), and end (MJD 56399) of the nine-day flaring activity. The bands represent the minimum and maximum value reached at each Lorentz factor, while the dashed lines depict the average.

The model describes the data within 30% for the vast majority of the bins in the 3–7 keV, 7–30 keV, 0.2–0.4 TeV, 0.4–0.8 TeV, and >0.8 TeV bands. The 3–7 keV and 7–30 keV bands are by far the ones that are the best reproduced. They respectively show a data/model mismatch below 15% for ≈90% and ≈80% of the bins. This is an expected behavior, given that the l_e and p variations are applied directly based on the 3–7 keV NuSTAR measurements, but these results provide an important validation of the procedure adopted for the parameter variations. Hence, any mismatch noticed in the other bands is likely caused by more fundamental aspects related to the model itself, like the choice of varying parameters and/or the initial modeling setup.

For the highest X-ray energies, 30–80 keV, there is a data/model mismatch at level of 50% on average during the first 5 days of the flare (MJD 56393 to MJD 56397). For the other days, the 30–80 keV emission is captured reasonably well by the model. The mismatch appears as a systematic underestimation of the flux, whereas the relative variations are preserved well by the model. The 30–80 keV range probes the most energetic part of the electron distribution, close to the cutoff γ_{max} (see Equation (2)). The underestimation likely originates from an inaccurate modeling of the shape of the exponential cutoff. Because these electron energies are probed by the high-energy edge of the NuSTAR bandwidth (covered by one or two spectral points at most), it is hardly possible to constrain a more complex shape of the cutoff than the one used here (see Equation (2)). In Section 5, we discuss ways to resolve this systematic difference.

In the VHE bands, the data/model match is mostly within 30%. Such a mismatch is also comparable to the systematics expected for MAGIC and Cherenkov telescopes in general for a Crab-like spectrum (J. Aleksić et al. 2016). A systematic underestimation of the fluxes is happening for the last few bins of MJD 56393. Over this time window, however, the 3–7 keV and 7–30 keV emissions are reproduced well. Variations of additional parameters (on top of p and l_e) are thus necessary to counteract the decrease of the VHE flux. It may also indicate the presence of an additional, unaccounted, subdominant emitting region not included in the current scenario. We stress that tuning the parameters of the "slow" zone will not help in this regard, since the systematic underestimation is also present at >0.8 TeV energies where the flux of the "slow" component is largely subdominant.

We now compare the spectral evolution of the model with the results of Section 3. To do so, we fit the model curves with the same spectral shape applied to the data, i.e., a log-parabola with curvature fixed to $\beta = 0.38$ for the X-ray and $\beta = 0.40$ for the VHE. At VHE, the fit also takes into account measurement uncertainties by simulating the MAGIC instrument response using the sensitivity curves from J. Aleksić et al. (2016). Figure 14 shows the photon indices $\alpha_{\text{X-ray}}$ and α_{VHE} plotted versus the 3–7 keV flux for the X-ray band and versus the >400 GeV flux for the VHE band, respectively, as in Section 3. The comparison is only performed over simultaneous MAGIC/NuSTAR time windows, because, at the

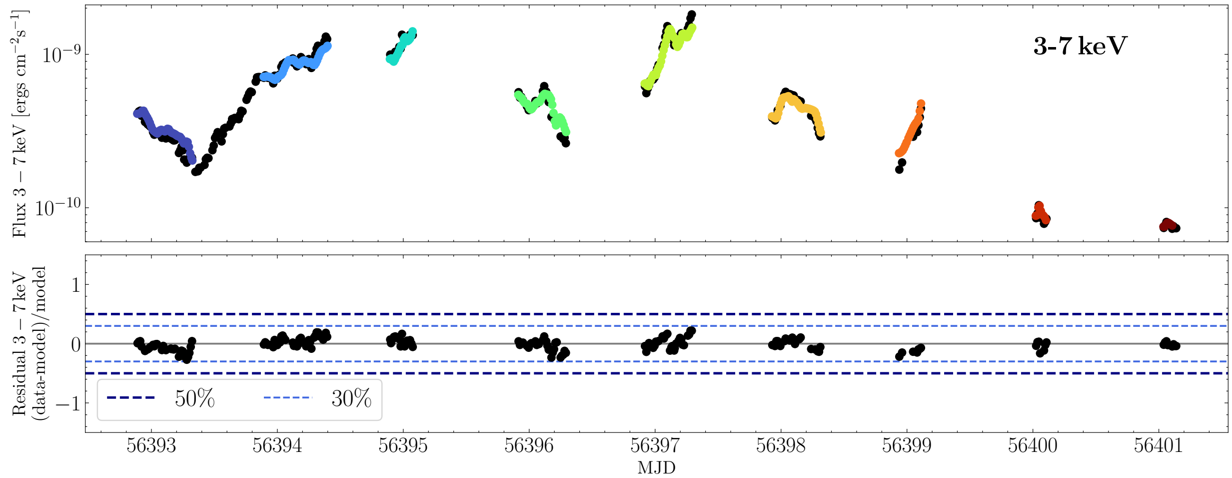

(a)

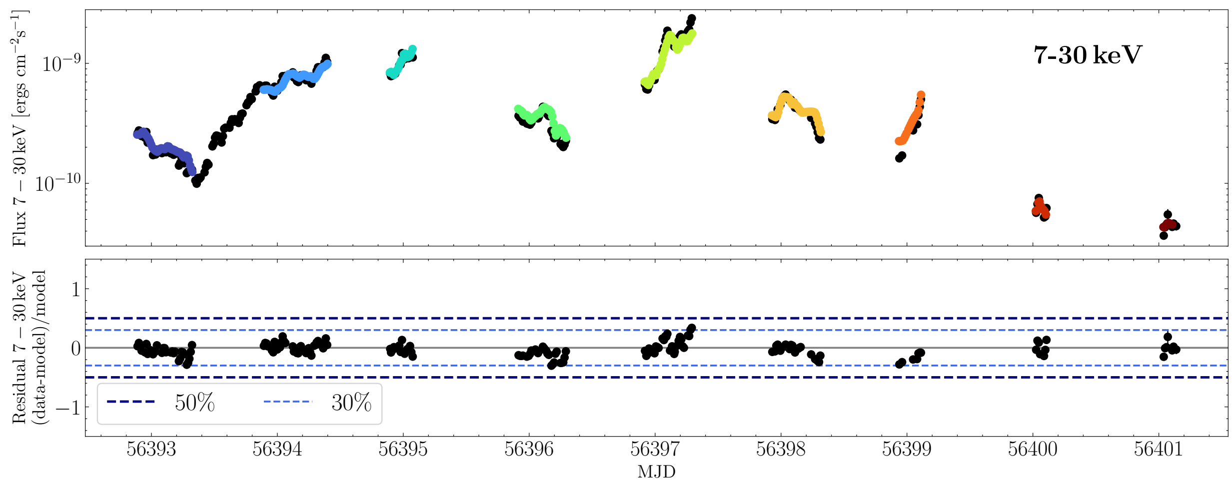

(b)

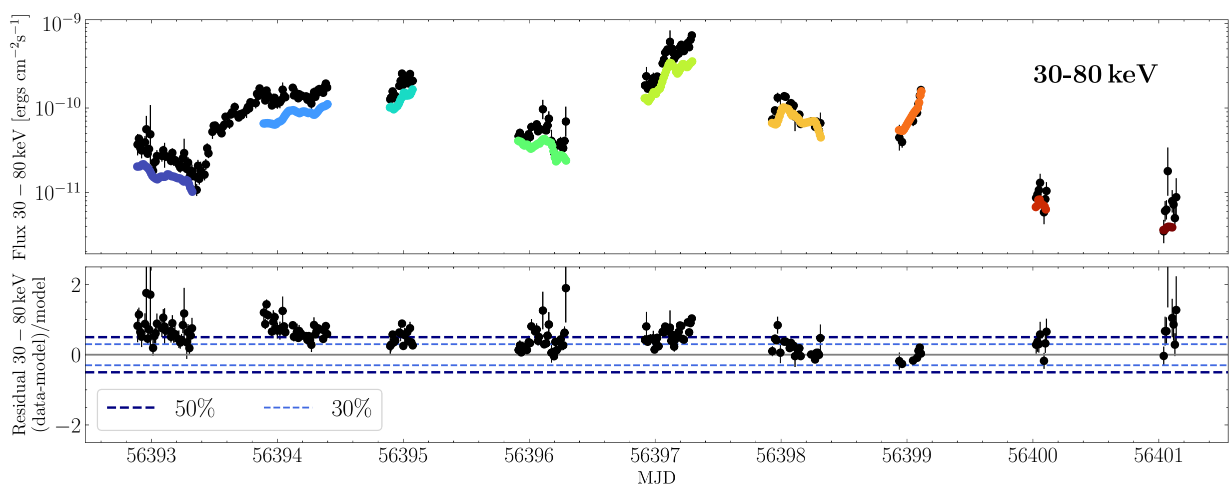

(c)

Figure 10. Comparisons between the light curve obtained from observations and light curves provided by the model. Solid colorful markers are the fluxes derived from the model, while dark points represent the data. From top to bottom: (a) 3–7 keV band (b) 7–30 keV band, and (c) 30–80 keV band. The bottom panel of each subplot shows the residuals, defined as $\frac{\text{(data − model)}}{\text{model}}$.

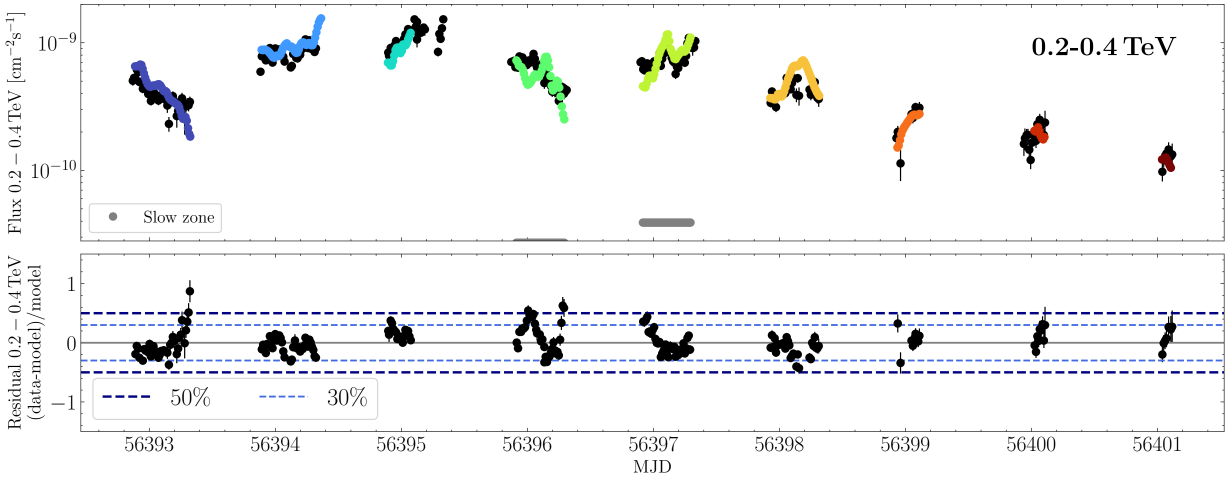

(a)

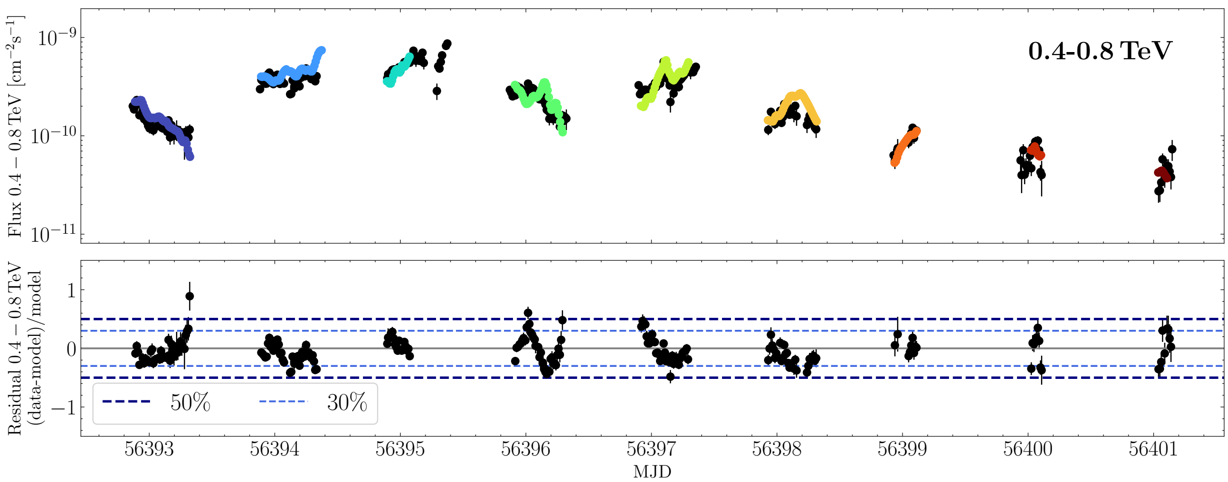

(b)

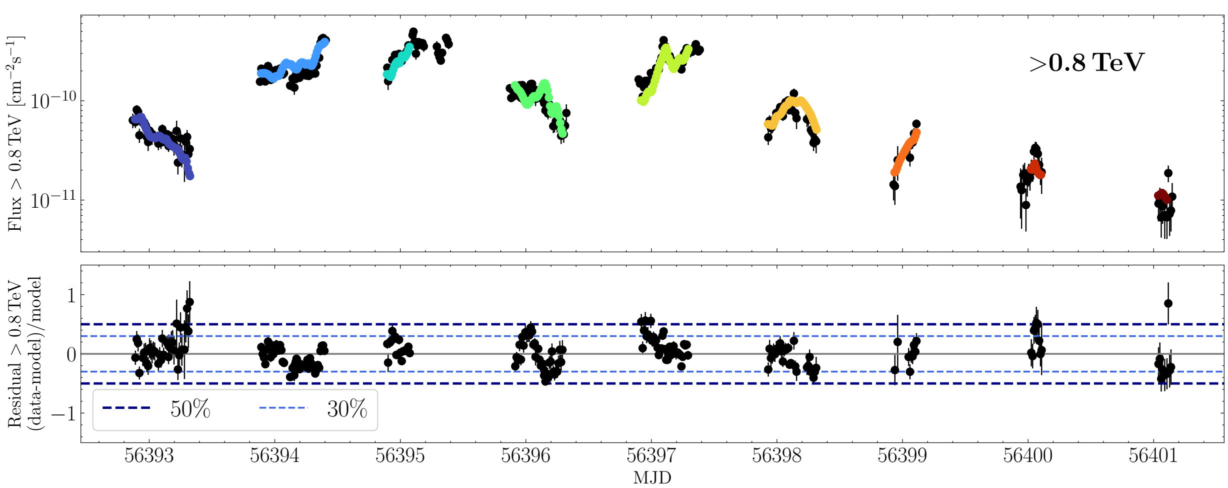

(c)

Figure 11. Same as Figure 10, but at (a) > 0.8 TeV (b) 0.4–0.8 TeV, and (c) 0.2–0.4 TeV energies. For the 0.2–0.4 TeV and 0.4–0.8 TeV bands, we further show (with gray markers) the flux from the "slow" component, which brings a small contribution to the total flux on MJD 56397. For the other days, as well as for the entire 0.2–0.4 TeV and >0.8 TeV light curve, the "slow" zone contribution is completely negligible and therefore omitted from the plot.

moment, the publicly available VERITAS results from this 2013 April flare of Mrk 421 only relate to the multiband light curves (W. Benbow & VERITAS Collaboration 2017).

In the X-rays, the model hardness is in good agreement with the data, and α differs at most by $\sim$10% from the measurements. In fact, the great majority of the bins agree

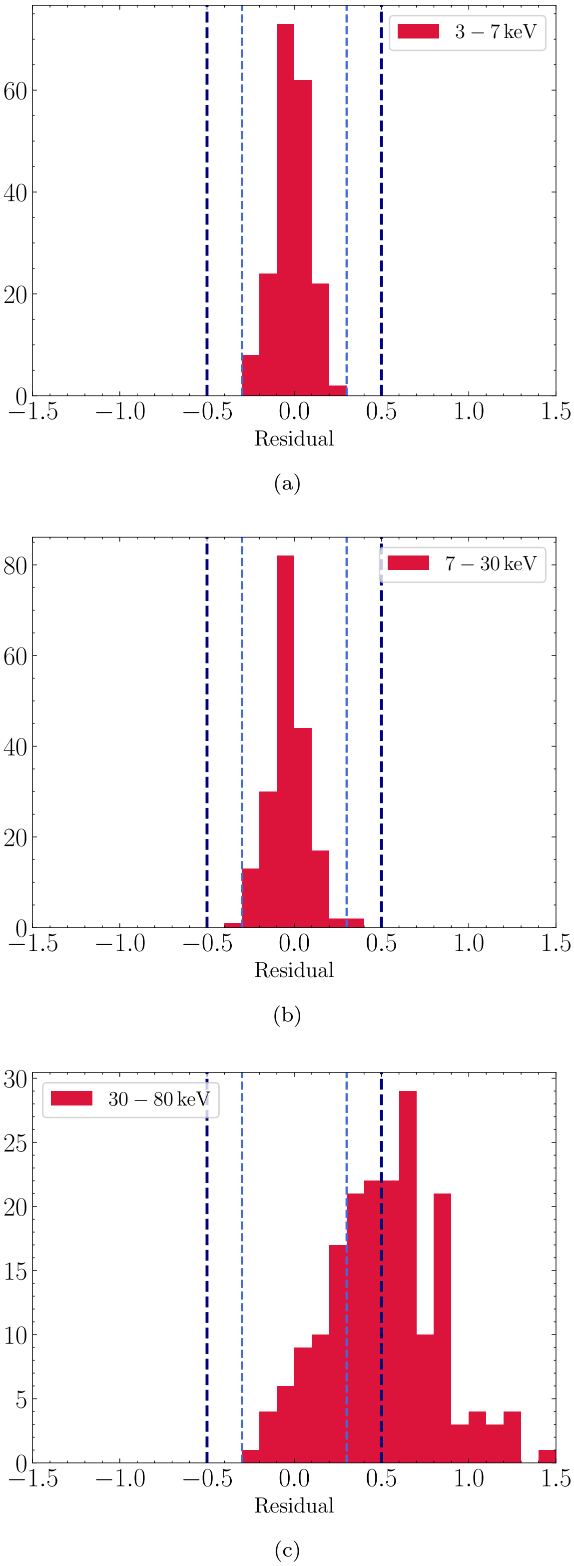

Figure 12. Histogram of the residuals, defined as $\frac{\text{(data} - \text{model)}}{\text{model}}$, for the three X-ray bands: (a) 3–7 keV (b) 7–30 keV, and (c) 30–80 keV.

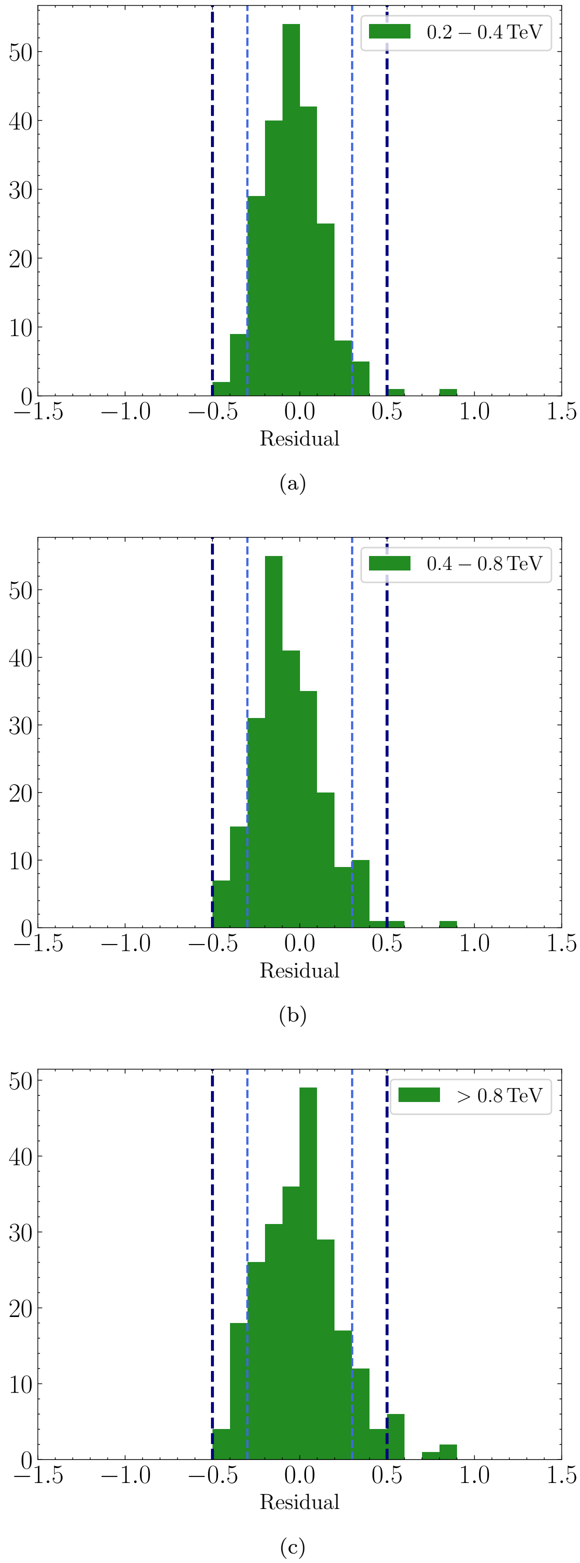

Figure 13. Same as for Figure 12, but for the three VHE bands: (a) 0.2–0.4 TeV, (b) 0.4–0.8 TeV, and (c) >0.8 TeV.

within 5%. A similarly good agreement is obtained for the VHE band, except for MJD 56397. For the latter day, VHE spectra from the model are significantly softer than the observations. Panel (b) of Figure 14 shows that the X-ray hardness is reproduced well for all the bins during MJD 56397, implying that the mismatch at VHE can hardly be solved by simply modifying the shape of the electron distribution. In Figure 15, we present a zoom-in on MJD 56398, during which an indication of an intraday hysteresis loop is visible.

Finally, we compare the model broadband SEDs with observations from the radio to VHE. SEDs in strictly simultaneous bins of 15 minutes are extracted from the

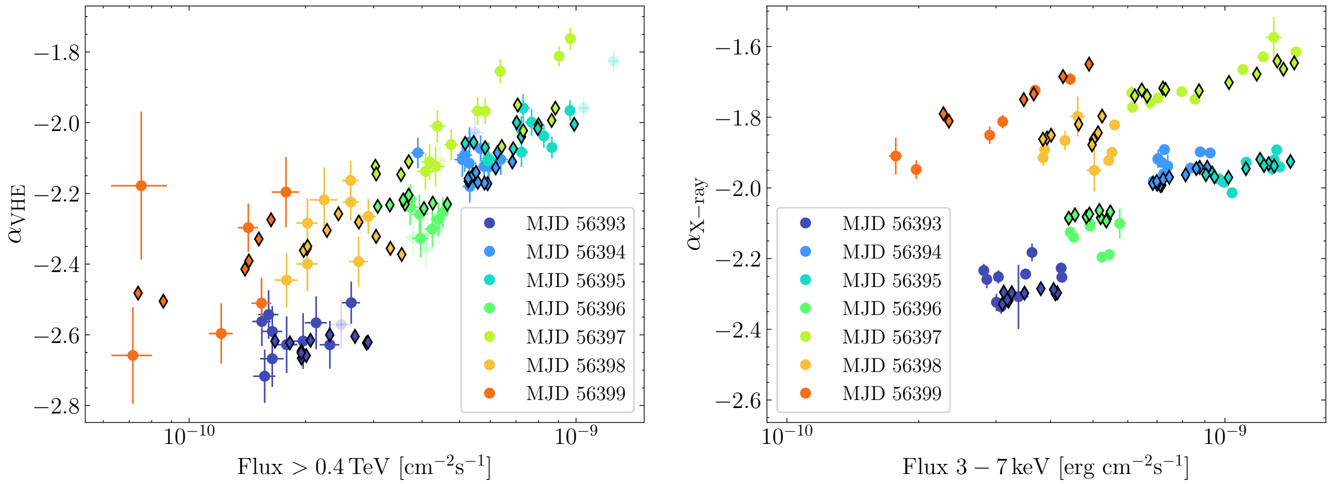

(a) (b)

Figure 14. Spectral parameter α as function of the flux for (a) MAGIC and (b) NuSTAR, as obtained from the data (circle marker) and from the model (solid diamond marker). Transparent markers in the VHE band depict measurements for which MAGIC does not have a strictly simultaneous NuSTAR measurements.

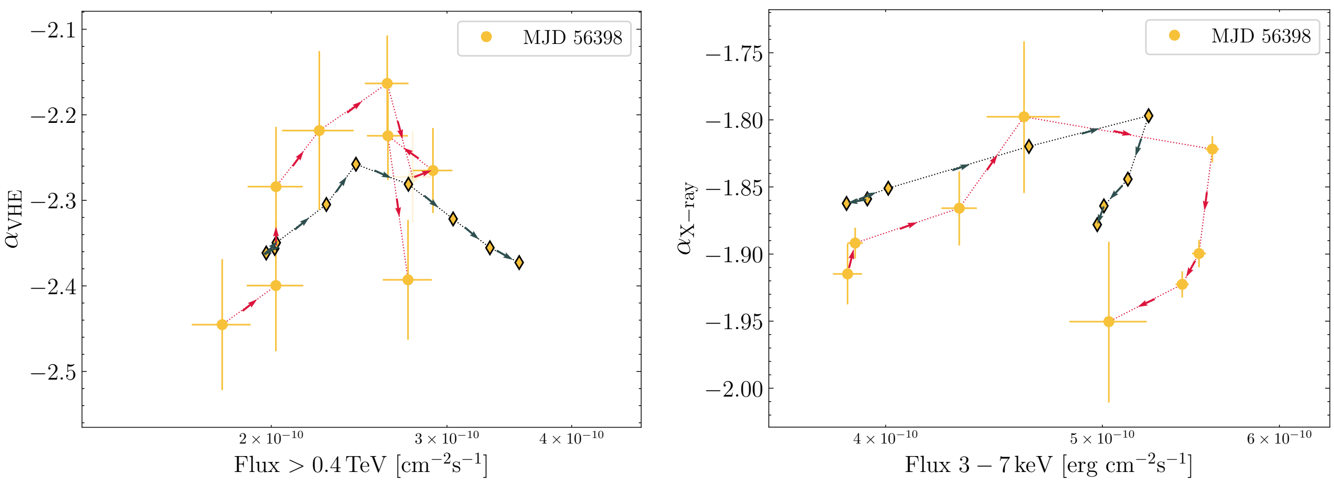

(a) (b)

Figure 15. Same as Figure 14, but zoomed in on MJD 56398, during which an indication of intraday spectral hysteresis is measured. Red and black arrows show the direction of time for the data and the model, respectively.

NuSTAR, MAGIC, and VERITAS data. The VERITAS SEDs are obtained in three energy bins by making use of the light curves quoted in Paper I: 0.2–0.4 TeV, 0.4–0.8 TeV, and >0.8 TeV. The SED point in each energy bin is placed at the mean energy weighted by the source spectral shape, using the spectral shape averaged over the flare[51] ($dN/dE \propto E^{-2.14-0.45\log_{10}(E/300\,{\rm GeV})}$; see Paper I). The Fermi-LAT SED values are averaged over 12 hr centered at the VHE measurements. With Mrk 421 being relatively faint in the Fermi-LAT band, this time binning provides a good trade-off between simultaneity and statistical uncertainty. At lower energies, SED points are computed in the radio, optical, and UV bands, using the light curves of Figure 17. We select observations that are the closest in time to the VHE/X-ray data, leading to a temporal offset of at most ∼5 hr from the VHE/X-ray measurements, below the observed variability timescale.

In total, we obtain 310 broadband SEDs that extend over the nine-day flaring activity, namely from April 11 until April 19 (MJD 56393–56401). Out of these 310 SEDs, 240 lie inside time intervals that contain a VHE and X-ray coverage, i.e., the intervals over which we apply our model. For convenience purposes, we only provide in this manuscript snapshots for each of the days in Figures 21 and 22 in Appendix F. The complete set of SEDs has been published online.[52]

5. Discussion

5.1. Spectral Hysteresis in the Temporal Evolution of the X-Ray and VHE Emissions

The NuSTAR data reveal hysteresis loops in clockwise direction (see Section 3). The loops occur on daily and subhour timescales, and they repeat during several days. Similar X-ray

[51] Since we do not take into account short-timescale spectral variability, we risk introducing some bias in the VERITAS SED points. Based on the spectral variability observed in the MAGIC data, we evaluate that this bias is expected to be, at most, on the level of the statistical uncertainty (∼10%) of the individual SED points.

[52] 10.5281/zenodo.17054582

spectral behavior has already been reported in Mrk 421 and other HBLs (T. Takahashi et al. 1996; Y. H. Zhang et al. 2002; A. D. Falcone et al. 2004; M. Ravasio et al. 2004; R. Sato et al. 2008; B. Kapanadze et al. 2016; A. U. Abeysekara et al. 2017). B. Kapanadze et al. (2016) investigated spectral hysteresis in X-ray data from Swift-XRT and NuSTAR during the period 2013 January to 2013 June and reported clockwise and counterclockwise loops, underlining the complex character of X-ray variability on a wide range of timescales. At VHE, the MAGIC spectra closely follow the patterns observed in the X-rays over the simultaneous time windows (see Figure 2 and Section 3). One of the most interesting features is the indication of a simultaneous X-ray/VHE clockwise loop on MJD 56398 (see Figure 2). Attempts to detect spectral hysteresis in VHE have been reported in the past (see, e.g., H. E. S. S. Collaboration et al. 2012; A. U. Abeysekara et al. 2017), but with no success, likely due to lack of statistics. To our knowledge, this is the first time that structured spectral trends going beyond the usual harder-when-brighter evolution have been detected at VHE in a blazar flare. The similarities in the evolution of the VHE and X-ray hardness indicate the need for a common underlying particle population, hence favoring the SSC model (L. Maraschi et al. 1992).

Hysteresis loops in a clockwise direction are caused by a lag of the lower-energy photons with respect to the higher-energy ones. It can be interpreted as a signature of synchrotron cooling (J. G. Kirk et al. 1998). Under this assumption, δ and B are constrained as (Y. H. Zhang et al. 2002)

$$B\delta^{1/3} = 209.91\left(\frac{1+z}{E_l}\right)^{1/3}\left(\frac{1-(E_l/E_h)^{1/2}}{t_{\rm delay}}\right)^{2/3}, \quad (7)$$

where $t_{\rm delay}$ is the time delay (in s), E_l and E_h are the lower and higher photon energies (in keV) between which the delay is observed, B is the magnetic field strength in Gauss, and z is the redshift. In order to make rough estimates, we set $E_l = 3$ keV and $E_h = 15$ keV, which are respectively the start energy and the logarithmic mean energy used in the NuSTAR fits, and $t_{\rm delay} \approx 1$ hr is the timescale of the hysteresis loops observed on MJD 56398. Setting $\delta = 100$, as used in the "fast" zone, one finds $B \sim 0.09$ G. This is very close to the values adopted in the time-dependent model (see Table 2). Nonetheless, for such a magnetic field strength, and assuming that electrons escape on timescales $t_{\rm esc} = R/c$ (where $R \sim 10^{15}$ cm is the radius of the "fast" zone), the synchrotron cooling break lies at $\log\gamma_{\rm syn,break} \sim 6.2$, which is beyond $\gamma_{\rm max}$ for all days. Synchrotron cooling therefore does not significantly affect the flux variations in our model, and the evolution of the particle distribution is predominantly dictated by the acceleration/injection and escape process. Note that the particle cooling from inverse Compton scattering remains subdominant.

If the escape timescale is substantially increased to $t_{\rm esc} \sim 10\,R/c$, synchrotron cooling may affect the shape of the electron distribution because, under such conditions, $\gamma_{\rm syn,break} \lesssim \gamma_{\rm max}$. If the particles are contained in a blob of highly turbulent plasma, the escape timescale is related to the diffusion timescale (P. A. Becker et al. 2006), which can in principle be an order of magnitude longer than *R/c*. However, as argued in Section 4.1.1, the large Doppler factors and the stability of the source parameters throughout the flare favor an emitting region behind a stationary shock. In such a scenario, the escape timescale is given by the advection velocity ($v_{\rm adv}$) of the plasma, leading to $t_{\rm esc} \sim R/v_{\rm adv} \sim R/c$ (since $v_{\rm adv} \sim c$).

5.2. Particle Dynamics and Acceleration Processes

The subhour variations in X-ray and VHE bands are reproduced well by varying two parameters: the electron luminosity and the slope of the injected distribution. The fluxes match the data within ∼30%, and for the vast majority of the time bins, the photon index agree within <0.2 (equivalent to <10%; see Figure 14).

We cannot exclude that other combinations of parameters in the "fast" zone are able to explain the X-ray and VHE variability. Nonetheless, variations of p constitute a minimal requirement to explain the subhour spectral variations discussed in Section 3, and the changes in p are also implied by the chromatic behavior of the X-ray/VHE correlation (see Paper I). Furthermore, spectral variability cannot be reproduced with synchrotron cooling only, because the changes in the spectral indices are not monotonic. Variations of $\gamma_{\rm max}$ may lead to an evolution of the X-ray/VHE photon indices and fluxes (as proposed in A. Mastichiadis & J. G. Kirk 1997; M. Petropoulou 2014), but in our case this is not sufficient. Indeed, from the stationary states (see Table 2), one finds $\log\gamma_{\rm max} \sim 5.2 - 5.4$. Due to the Klein–Nishina suppression effects, changes of $\gamma_{\rm max}$ around such high Lorentz factors will not be able to generate the intraday spectral variation of $\Delta\alpha_{\rm VHE} \approx 0.3$–$0.4$ measured at VHE (see Figure 2).

The evolution of l_e (or equivalently $L_{\rm e}$) dominates the intraday flux variability in our model, but rapid fluctuations of B may also have a significant contribution, since $L_{\rm SSC} \sim L_{\rm syn} \sim B^2$. However, a smaller inverse Compton variability will be induced compared to the scenario with varying l_e given that $L_{\rm SSC} \sim L_{\rm syn}^2 \sim l_e^2$. If only the magnetic field strength varies, it will thus underproduce the observed VHE variability and additional varying parameters would be needed to compensate this. In summary, our investigations favor p and l_e as the minimal combination of parameters able to capture the spectral and flux variations.

We present in Figure 16 the correlation plot of p and l_e. For clarity, the data points are binned over 15 minutes, similar to the observed light curves. An evident (anti)correlation is visible, implying a particle distribution that becomes harder when the electron density increases. This is expected from the general harder-when-brighter trend visible in the hardness versus flux plots presented in Section 3.

Magnetic reconnection is, in general, favored with respect to shocks to explain fast variability. A fraction of the magnetic energy is transferred to bulk kinetic energy of plasmoids formed in the reconnection layer, leading to the production of plasmoids moving at relativistic speeds with respect to the jet's comoving frame. As a result, the emitting regions have an effective Doppler factor reaching up to $\delta \sim 100$, as used here for the "fast" zone (D. Giannios et al. 2009; D. Giannios 2013; M. Petropoulou et al. 2016). J. Jormanainen et al. (2023) compared predictions of magnetic reconnection using PIC simulations with the flux variability patterns observed in the 2013 flare of Mrk 421. The authors derived a spread in the model photon index of $\Delta\Gamma \approx 0.4$, equivalent to a spread in the electron power-law slope of ≈0.8 (see Equation (E1)). This amplitude is significantly lower than the one derived in this work that would be necessary to match the spectral changes in the data ($\Delta p = 1.8$). We note that J. Jormanainen et al. (2023)

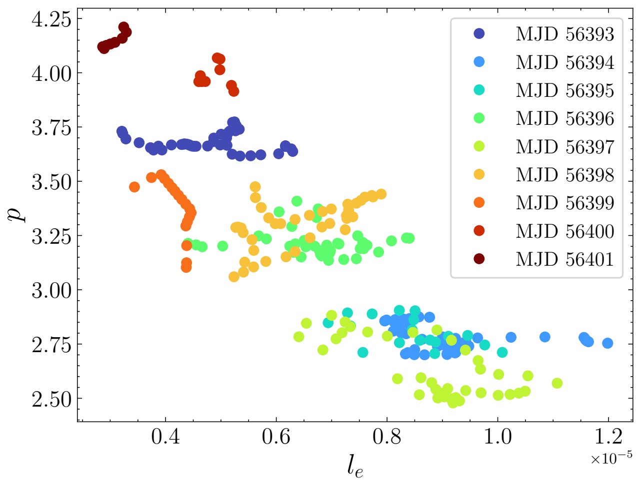

Figure 16. Correlation between the p and l_e parameters of the electron distribution injected in the "fast" zone for the time-dependent modeling described in Section 4. The data are binned in 15 minute intervals.

adopted a fixed magnetization[53] of $\sigma = 50$, while the power-law slope of particles accelerated in reconnection events scales with the magnetization of the plasma (see, e.g., L. Sironi et al. 2016). Based on 2D PIC reconnection simulations presented in L. Sironi & A. Spitkovsky (2014), the particle distribution index approaches $p \approx 4$ for a plasma magnetization of $\sigma = 1$ and $p \approx 2$ for $\sigma = 10$. Since $\sigma \propto B^2$, this means that the magnetic field should vary by a factor of a few to explain the amplitude in p. In our model, B varies by less than a factor of 2 between the days (see Table 2), and hence is somewhat at odds with a reconnection scenario. Finally, in Paper I, we showed that, to explain some of the broad features like the flux doubling time in the X-rays, $\sigma \approx 10$ had to be assumed (the bulk velocity of the plasmoids scales as $\sim\sqrt{\sigma}$), which would imply much harder indices p than derived in our model.

Relativistic plasma shocks constitute an alternative efficient acceleration mechanism (J. G. Kirk & P. Duffy 1999). In this case, the slope of the particles sensitively depends on the shock compression ratio r, or equivalently, the ratio $t_{\rm acc}/t_{\rm esc}$, where $t_{\rm acc}$ is the acceleration timescale (J. G. Kirk et al. 1998; U. Keshet & E. Waxman 2005; J. J. P. Virtanen & R. Vainio 2005). Using Equation (2) from J. J. P. Virtanen & R. Vainio (2005), which is a good approximation of the index generated by relativistic parallel shocks of finite thickness, one finds that variations of r by only a factor of $\sim$2 can easily lead to modification of the slope from $p \approx 2.5$ to $p \approx 4$, as in Figure 16. From this point of view, diffusive shock acceleration is favored over magnetic reconnection.

As mentioned in Section 4.1.1, the model parameters suggest emission regions from quasi-stationary features, which may be indicative of recollimation shocks. To stay subdominant in the optical band (as suggested by the absence of X-ray and optical correlation) and to satisfactorily describe the SED, the "fast" zone must have a minimum Lorentz factor of $\gamma_{\rm min} \sim 10^4$. As discussed in A. Zech & M. Lemoine (2021), such large values of $\gamma_{\rm min}$ are generally possible in cases of electron–proton coacceleration at shocks, but would be puzzling in the specific case of recollimation shocks. Indeed, in the latter scenario, the minimum electron Lorentz factor is approximated as $\gamma_{\rm min} \approx 1200\,\Gamma_{\rm j}/\delta_{\rm fast}$ (A. Zech & M. Lemoine 2021), where $\Gamma_{\rm j}$ is the jet Lorentz factor. This implies $\Gamma_{\rm j} \sim 10^3$, in tension with constraints from very long-baseline interferometry (VLBI) observations that typically yield $\Gamma_{\rm j}$ of a few tens. We note, however, that D. C. Homan et al. (2021) found extreme rare cases with $\Gamma_{\rm j} \sim 10^2$–10^3 on parsec scales in some AGN jets with MOJAVE and 2 cm Survey programs at 15 GHz. These extreme cases are mostly found among flat spectrum radio quasars, while BL Lac–type objects seem to saturate at $\Gamma_{\rm j} \lesssim 10^2$.

To relax these extreme jet requirements and at the same time explain the high $\gamma_{\rm min}$, a possibility is to invoke pre-acceleration processes. For instance, a sequence of standing shocks may successively increase $\gamma_{\rm min}$ as long as particles do not cool efficiently (and produce detectable radiation) when traveling between each shock (A. Zech & M. Lemoine 2021). O. Hervet et al. (2019) also investigated this scenario to interpret the repetitive X-ray flaring episode in Mrk 421. Interestingly, the latter analysis constrained jet parameters to values consistent with the "fast" zone (i.e., $\Gamma_b \in [43 - 66]$, $\delta > 32$).

5.3. Caveats and Shortcomings of the Model

The model assumes two distinct, noninteracting emitting regions, possibly associated with stationary shocks. As argued in Section 4.1.1, if the two regions are separated by more than a few $\sim 10^{16}$ cm ($\sim 10^{-2}$ pc), it is well-justified to neglect in each component the interaction of particles with the radiative field from the other region. Therefore, such a configuration effectively leads to two "one-zone" SSC models. As shown in F. Tavecchio & G. Ghisellini (2016), large Doppler factors (higher than VLBI constraints) and low magnetic field are general features of one-zone models. A possible solution to solve this "Doppler crisis" is to consider a stratified region, where the plasma flows with a higher Lorentz factor close to the jet base and then drops further downstream the jet (as in a decelerating flow). The region may also be radially stratified and consist of a central component of the jet that possesses a fast plasma flow (the spine) surrounded by a slower layer (the sheath). In both cases, the interaction and the relative motion between the emitting regions could result in a lower δ and higher B, while capturing satisfactorily the synchrotron and inverse Compton components. This was extensively discussed in earlier works, e.g., in M. Georganopoulos & D. Kazanas (2003) and G. Ghisellini et al. (2005).

A time-dependent model with interacting emitting regions is beyond the scope of this paper, and it demands a significantly higher degree of complexity. Indeed, the particle distributions in the different components need to be evolved simultaneously after incorporating the mutual interplay of their radiation fields. Assuming that an interacting stratified scenario indeed allows for a larger B compared to our model, the synchrotron cooling timescale may be sufficiently shortened to impact the evolution of the particle distribution, thus modifying the conclusions from the previous section regarding the origin of the hysteresis loops (which we attribute to the acceleration/injection process). An increase of B by a factor of $\sim$3 (while keeping $R \sim 10^{15}$ cm and $t_{\rm esc} \sim R/c$), is sufficient to obtain $\gamma_{\rm syn,break} \lesssim \gamma_{\rm max}$. V. A. Acciari et al. (2020b) showed that such a difference in B is possible between homogeneous and spine-sheath scenarios. However, a dedicated modeling is necessary to precisely quantify to what extent δ and B can be modified with respect to Table 2.

[53] $\sigma = B^2/4\pi mnc^2$, where n is the electron number density.

We anticipate that a stratified/interacting model will only marginally affect most of our conclusions. First, the correlation between l_e and p in Figure 16 will remain largely unchanged, as well as the need for $\gamma_{\rm min} \sim 10^4$ in the "fast" zone to stay subdominant in the optical band. Moreover, assuming very conservatively that a stratified region allows for a reduction of $\delta_{\rm fast}$ by an order of magnitude, an emitting region would travel on $\Delta d \sim \frac{\Gamma^2_{\rm b,fast}\delta_{\rm fast} c \Delta T_{\rm obs}}{1+z} \sim 10^{18}$ cm over the flaring episode, equivalent to ∼pc scales, which is again at odds with the stability of the parameters of the stationary states. Hence, recollimation shocks would still be favored, as opposed to a blob-in-jet scenario. Finally, an order-of-magnitude lower Doppler factor demands $\Gamma_{\rm j} \sim 10^2$ in order to obtain $\gamma_{\rm min} \sim 10^4$ ($\gamma_{\rm min} \approx 1200\, \Gamma_{\rm j}/\delta_{\rm fast}$) for electron–proton coacceleration on a recollimation shock, which is still higher than VLBI observations.

On MJD 56397, the VHE hardness predicted by the model is clearly softer than in the data (see left panel of Figure 14). Since the X-ray spectrum is reproduced well (see right panel of Figure 14), the mismatch at VHE cannot be resolved by only modifying the parameters of the electron distribution. Instead, this may be indicative of the emergence of short-lived additional emitting regions filled with highly energetic electrons, which are currently ignored in our model. The origin of these extra components remains unclear. Ultra-fast plasmoids (that are short-lived for the observer) can be easily produced in a magnetic reconnection scenario (D. Giannios et al. 2009; D. Giannios 2013; M. Petropoulou et al. 2016). On the other hand, as already mentioned, our model parameters (and their stability over time) tends to favor shocks as the acceleration mechanism.

We conclude this section by discussing a general shortcoming of our model: a systematic underestimation of the 30-80 keV fluxes from NuSTAR. Although the relative flux variations are preserved well by the model, the fluxes are lower than the observations by roughly 50% on average from MJD 56393 to MJD 56397. Given that the X-ray photon indices are reproduced well by the model (within 10%; see Figure 14), this mismatch points toward a nonoptimal description of the electron distribution close to $\gamma_{\rm max}$. Although we deem the systematic flux offset relatively mild in light of the complexity of the emission patterns during the flare, as well as the spectral shapes and the rest of the fluxes in the other subenergy bands being well-reproduced, these NuSTAR observations constitute one of the very few data samples providing a precise measurement of the 30–80 keV subhour variability in HBLs. Hence, we investigated alternative parameterization of the exponential cutoff, to see if the discrepancy can be resolved.

To enhance the synchrotron emission above 30 keV, we softened the sharpness of the cutoff by lowering a in the electron distribution ($\propto \gamma^{-p} \exp(-(\gamma/\gamma_{\rm max})^a)$; see Equation (2)). We find that $a = 1.5$ instead of $a = 2$ provides a reasonable description of the 30–80 keV fluxes, together with the other X-ray and VHE bands. However, the X-ray spectral index $\alpha_{\rm X-ray}$ becomes systematically harder by $\Delta\alpha_{\rm X\text{-}ray} \approx 0.15$. Thus, $a = 1.5$ results in an overall degradation of the X-ray spectra compared to the $a = 2$ model (see Figure 14). The VHE spectra remained unchanged, mostly due to the Klein–Nishina suppression of the inverse Compton scattering from electrons close to the cutoff. Additionally, we enhanced the 30–80 keV emission after increasing $\gamma_{\rm max}$ by 0.1 dex (being the particle grid resolution used in the code). As in the previous case, the 30–80 keV fluxes can be captured well, but the X-ray spectra become significantly harder than the data.

In conclusion, an optimal description of the 30–80 keV fluxes (i.e., within $\lesssim$50%) cannot be achieved with the current parameters of our model, if one wants to preserve a good description of the NuSTAR photon indices. A more complex shape of the high-energy cutoff in the electron distribution may be needed, but since the 30–80 keV energy range is only covered by one or two NuSTAR SED points, a model with more degrees of freedom than Equation (2) can hardly be constrained. Nonetheless, it is interesting to note that our model prefers $a \approx 2$ rather than $a \approx 1$. This is in agreement with results from C. Baheeja et al. (2024) that fitted a sample of NuSTAR observations from Mrk 421.

6. Conclusions

The TeV blazar Mrk 421 exhibited substantial flaring activity in 2013 April, marking one of the largest outbursts recorded to date. This event was extensively monitored over nine consecutive days (April 11–19) by MAGIC, VERITAS, and NuSTAR, in conjunction with observations from Swift, as well as optical and radio telescopes. The intraband correlations and variability were thoroughly analyzed in Paper I. In the study reported in this paper, we extended our work by characterizing the simultaneous VHE and X-ray spectral evolution. We subsequently modeled the broadband evolution on a 15 minute scale using a time-dependent approach to accurately track the history of the particle distribution.

The high flux and rich multiwavelength coverage enabled the construction of 240 broadband SEDs throughout the nine-day flaring period on which the model was applied. We stress that, in most of the previous works on blazar flares that were modeled with a time-independent radiation code, the time variations were described on daily or longer timescales (see, e.g., A. U. Abeysekara et al. 2017; H. E. S. S. Collaboration et al. 2020; MAGIC Collaboration et al. 2020, 2021b). The key findings from our work are as follows:

1. The NuSTAR data in the X-ray band reveal spectral hysteresis loops in a clockwise direction at various intervals during the flare, indicating a behavior that exceeds a simple harder-when-brighter correlation.
2. In the VHE band, MAGIC spectra extend to energies exceeding 10 TeV. The evolution of spectral hardness in the VHE band closely follows that in the X-ray band. For the first time, we report evidence of concurrent clockwise VHE spectral hysteresis alongside the X-ray emission. The simultaneous spectral trends in the X-ray and VHE bands strongly support leptonic models for the origin of the gamma-ray emission.
3. Our time-dependent leptonic modeling demonstrates that the majority of the subhour variations in flux and spectral characteristics can be explained by changes in the luminosity and the slope of the injected electron distribution.
4. Our model indicates that the magnetic field remains stable, varying by less than a factor of two, while the size of the emitting region remains constant. The small variations of the source environment support an emitting region behind a standing shock within the jet, such as recollimation shocks.

5. The model's derived variations in the slope of the electron distribution could occur within a shock-acceleration scenario if the shock compression ratio changes by a factor of approximately 2. In contrast, a magnetic reconnection model would necessitate significant changes in plasma magnetization, which contradicts the stable magnetic field characteristics observed in our model.
6. To accurately reproduce the VHE data at the highest energies, a Doppler factor δ close to 100 is required. In a standing shock scenario, as indicated by the model parameters, this necessitates a jet Lorentz factor of $\Gamma_j \sim 10^3$ to achieve the necessary $\gamma_{min} \sim 10^4$. This large γ_{min} is suggested by the absence of strong variability in the optical/UV bands and their lack of correlation with the highly variable X-rays. The required high jet velocity of $\Gamma_j \sim 10^3$ significantly exceeds typical values obtained from VLBI observations. While the Doppler factor could be reduced by assuming interactions between the radiation fields of compact and extended regions, even in this scenario, a Lorentz factor of at least $\Gamma_j \sim 100$ would still be necessary within the standing shock framework to achieve $\gamma_{min} \sim 10^4$.

Acknowledgments

We would like to thank the Instituto de Astrofísica de Canarias for the excellent working conditions at the Observatorio del Roque de los Muchachos in La Palma. The financial support of the German BMFTR, MPG, and HGF; the Italian INFN and INAF; the Swiss National Fund SNF; the grants PID2019-107988GB-C22, PID2022-136828NB-C41, PID2022-137810NB-C22, PID2022-138172NB-C41, PID2022-138172NB-C42, PID2022-138172NB-C43, PID2022-139117NB-C41, PID2022-139117NB-C42, PID2022-139117NB-C43, PID2022-139117NB-C44, and CNS2023-144504 funded by the Spanish MCIN/AEI/ 10.13039/501100011033 and "ERDF A way of making Europe"; the Indian Department of Atomic Energy; the Japanese ICRR, the University of Tokyo, JSPS, and MEXT; the Bulgarian Ministry of Education and Science, National RI Roadmap Project DO1-400/18.12.2020, and the Academy of Finland grant No. 320045 are gratefully acknowledged. This work has also been supported by Centros de Excelencia "Severo Ochoa" y Unidades "María de Maeztu" program of the Spanish MCIN/AEI/ 10.13039/501100011033 (CEX2019-000920-S, CEX2019-000918-M, and CEX2021-001131-S) and by the CERCA institution and grants 2021SGR 00426 and 2021SGR 00773 of the Generalitat de Catalunya; by the Croatian Science Foundation (HrZZ) Project IP-2022-10-4595 and the University of Rijeka Project uniri-prirod-18-48; by the Deutsche Forschungsgemeinschaft (SFB1491) and by the Lamarr-Institute for Machine Learning and Artificial Intelligence; by the Polish Ministry Of Education and Science grant No. 2021/WK/08; and by the Brazilian MCTIC, the CNPq Productivity grant 309053/2022-6, and FAPERJ grants E-26/200.532/2023 and E-26/211.342/2021. A.A.-E. and D.P. acknowledge support from the Deutsche Forschungsgemeinschaft (German Research Foundation) under Germany's Excellence Strategy—EXC-2094—390783311. M.P. acknowledges support from the Hellenic Foundation for Research and Innovation (H.F.R.I.) under the "2nd call for H.F.R.I. Research Projects to support Faculty members and Researchers" through the project UNTRAPHOB (Project ID 3013).

Data Availability

The broadband SEDs (from radio to TeV) in the 15 minute intervals throughout the entire flare are made available at the Zenodo repository DOI: 10.5281/zenodo.17054582. The repository also includes the SED models and the comparison with the data for all 15 minute bins, together with an animation illustrating the temporal evolution.

All the MAGIC data used in this work are further released in the Data Level 3 (DL3) format in order to be analyzed with the `gammapy` open source software (A. Donath et al. 2023). The DL3 files are available at the Zenodo repository DOI: 10.5281/zenodo.17064461, and they are released as part of the "ACME" MAGIC Open Data-Analysis School.[54] Tutorials to process the DL3 files can be found in the following GitHub repository: https://github.com/magic-telescopes/acme_magic_odas/blob/master/3_light_curve_variable_source.ipynb.

Facilities: MAGIC, VERITAS, NuSTAR, Swift, OVRO, IRAM:30, Metsähovi Radio Observatory.

Software: MARS (R. Zanin et al. 2013), XSpec (K. A. Arnaud 1996), NuSTARDAS, XRTDAS, Fermitools (https://fermi.gsfc.nasa.gov/ssc/data/analysis/).

Author Contributions

A. Arbet-Engels: project leadership, MAGIC, Fermi-LAT & NuSTAR analysis, modeling, and paper drafting; A. Babić: MAGIC analysis crosscheck; D. Paneque: organization of the observations, coordination of the multiwavelength data reduction, and paper drafting; M. Petropoulou: modeling and paper drafting; M. Polkas: modeling and paper drafting. The rest of the authors have contributed in one or several of the following ways: design, construction, maintenance, and operation of the instrument(s) used to acquire the data; preparation and/or evaluation of the observation proposals; data acquisition, processing, calibration, and/or reduction; production of analysis tools and/or related MC simulations; and overall discussions about the contents of the draft, as well as related refinements in the descriptions.

Appendix A
Observations and Data Processing

In the radio, the observations were performed by the OVRO, Metsähovi, and IRAM 30 m telescopes. In the optical, the data were taken in the *R* band by telescopes belonging to the GLAST-AGILE Support Program (e.g., M. Villata et al. 2008, 2009; M. I. Carnerero et al. 2017) of the Whole Earth Blazar Telescope[55] (e.g., M. Villata et al. 2002, 2006; C. M. Raiteri et al. 2007, 2017). The measurements in the UV regime were performed by the Swift UV and Optical Telescope (P. W. A. Roming et al. 2005) in the UVW1, UVM2, and UVW2 spectral bands. The corresponding fluxes were directly taken from Paper I, and the data reduction method was reported in M. Baloković et al. (2016).

The soft X-ray (0.3–10 keV) measurements are from the Swift X-ray Telescope (XRT; D. N. Burrows et al. 2005) and the data processing is described in M. Baloković et al. (2016).

54 https://acme-magic-odas.sciencesconf.org/
55 http://www.oato.inaf.it/blazars/webt/

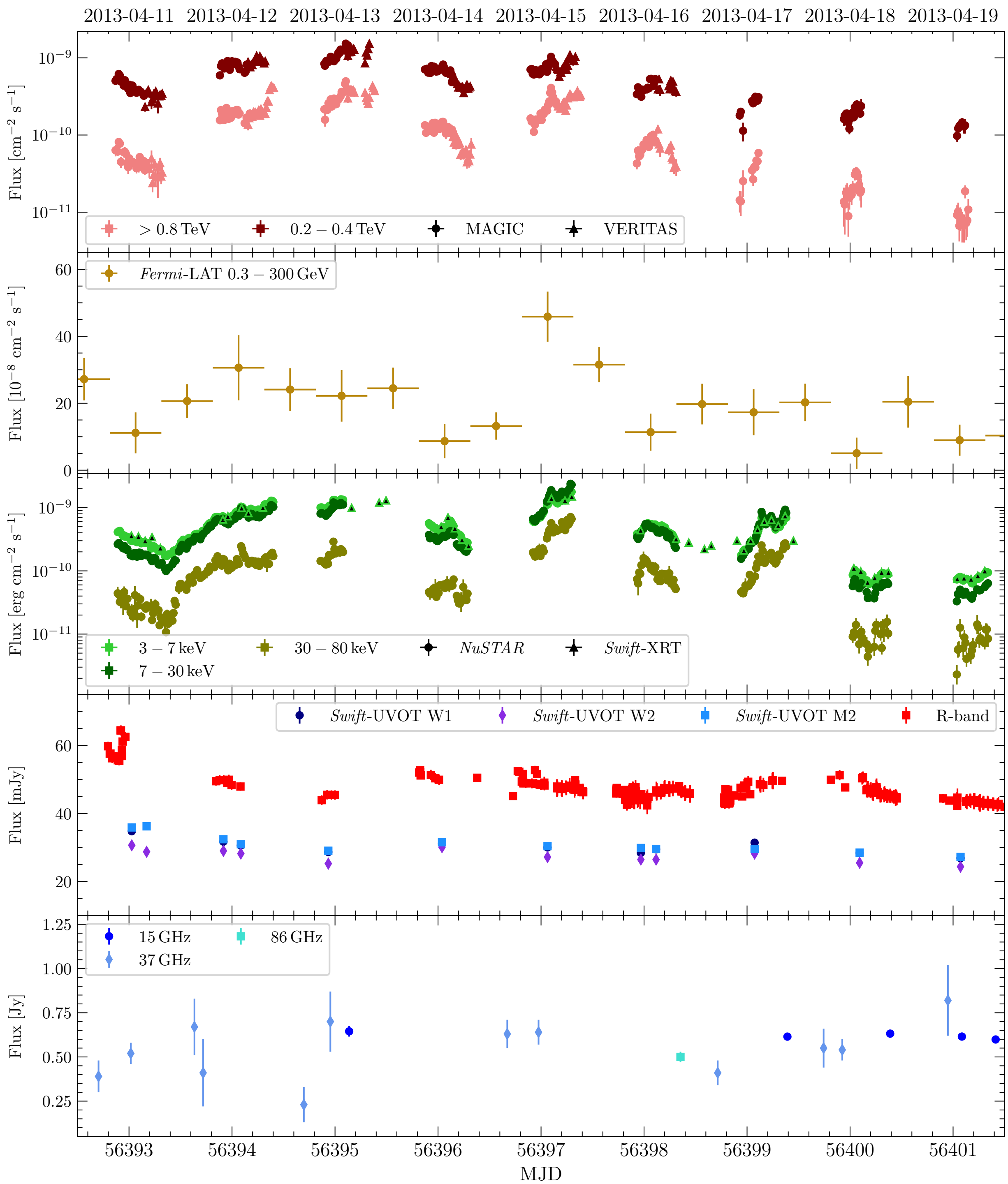

Figure 17. Multiwavelength light curves from VHE to radio frequencies during the 2013 April flare. Fluxes from MAGIC, VERITAS, Swift-XRT, Swift-UVOT, optical telescopes (R-band), and radio telescopes (15 GHz, 37 GHz, and 86 GHz) are directly taken from Paper I. Fermi-LAT and NuSTAR fluxes have been updated using more recent instrument response functions with respect to Paper I (see text in Appendix A for more details). The MAGIC, VERITAS, NuSTAR, and Swift-XRT light curves are binned in 15 minute intervals. The Fermi-LAT light curve is sampled homogeneously in identical 12 hr intervals. This binning differs slightly from the one adopted in Paper I, where the data were first divided into 12 hr intervals centered exactly at the VHE observations and then complemented by intervals where there are no VHE observations. The rest of the light curves are binned observation-wise.

In the hard X-ray band (3–79 keV), NuSTAR observed for about 70 hr during this flare. With respect to Paper I, the data were reprocessed with the NuSTARDAS software (version 2.1.1) using an updated CALDB version 20220215, which includes the major update in the effective area calibration released in 2021 October. As described in K. K. Madsen et al. (2022), this update leads to a systematic increase of the flux by ~5%–10% with respect to older CALDB versions. The events were screened from the effect of the south Atlantic anomaly using the options `tentacle=yes` and `saamode=optimized` in the `nupipepline` run. The source region was defined as a circular shape with a radius of ~100″ centered at the target. The background was extracted from an annulus around the target with an inner radius of ~120″ and an outer radius of ∼220″. To build broadband SEDs and calculate the fluxes, both Swift-XRT and NuSTAR data were independently fitted in Xspec (K. A. Arnaud 1996) with a log-parabola model and a column density $N_H = 1.92 \times 10^{20}\,\mathrm{cm}^{-2}$ (P. M. W. Kalberla et al. 2005). The spectra from the two NuSTAR focal plane modules (FPMA and FPMB) were modeled simultaneously adopting a cross-calibration normalization factor as a free parameter in the Xspec model. The resulting cross-normalization factor was almost exclusively in the order of a few percent, firmly within the expected systematics (F. A. Harrison et al. 2013). We fixed the pivot energy to 1 keV, as commonly adopted for Swift-XRT analysis, and to ease the comparison of the spectral parameters with recent works (e.g., MAGIC Collaboration et al. 2021a). We have verified that a pivot energy closer to the center of the NuSTAR bandwidth (for instance, 10 keV) does not change the NuSTAR fitting results.

The Large Area Telescope (LAT) on board the Fermi Gamma-ray Space Telescope (Fermi-LAT; W. B. Atwood et al. 2009; M. Ackermann et al. 2012) was used to characterize the emission in the MeV–GeV band. The Fermi-LAT data were reduced in a similar fashion as in Paper I, using the same analysis cuts and selecting the same region of interest (ROI) of 10° around Mrk 421. We adopted an updated version of the instrument response functions, P8R3_SOURCE_V3, instead of the P8R3_SOURCE_V2 that was used in Paper I. The diffuse Galactic and isotropic extragalactic background models[56] were included using the files gll_iem_v07.fits and iso_P8R3_SOURCE_V3_v1.txt, respectively. For the SEDs, we computed spectral points in each energy bin reaching a test statistic (TS; J. R. Mattox et al. 1996) above 5, and calculated an upper limit at a 95% confidence level otherwise. The data were reduced with the analysis software FERMITOOLS[57] (version 2.0.8).

At VHE, the MAGIC (J. Aleksić et al. 2016) observations were analyzed using the standard analysis tools from the MAGIC Analysis and Reconstruction Software package (R. Zanin et al. 2013; J. Aleksić et al. 2016). More details on the MAGIC observations and analysis can be found in Paper I. In this work, we simply extend the analysis of Paper I to extract SED points and spectral parameters at VHE. The spectra were fitted using a log-parabola model:

$$\frac{dN}{dE} = f_0 \left(\frac{E}{E_0}\right)^{\alpha - \beta \log_{10}\left(\frac{E}{E_0}\right)}, \tag{A1}$$

where f_0 is the normalization constant, α is the photon index, and β is the curvature parameter. The normalization energy E_0 was set to 500 GeV. All the SEDs and spectral parameters were evaluated after correcting for the extragalactic background light (EBL) absorption effects using the template described in A. Domínguez et al. (2011). Results of the spectral fits are presented in Section 3.

In order to extend and maximize the temporal coverage at VHE, we also make use of the VERITAS (J. Holder et al. 2008) data published in Paper I. Thanks to their different geographical locations, VERITAS and MAGIC observe one after another with a small overlap. This provides continuous VHE coverage over up to ∼10 hr day^{-1}. As detailed in Paper I, an energy-dependent systematic offset reaching up to 25%–30% was found between the MAGIC and VERITAS fluxes. Such an offset is within the expected instrumental systematics that are dominated by the uncertainty on the absolute energy scale. In fact, by assuming a shift by 20% of the MAGIC absolute energy scale, the SEDs from both instruments are compatible. To correct for the offset, the VERITAS fluxes in Paper I in each energy band were renormalized according to scaling factors determined assuming the 20% shift in the energy scale. In this work, we use the VERITAS light curves using the identical correction method.

The flux behavior was extensively discussed in Paper I. For completeness, we display in Figure 17 the multiwavelength light curves to provide a comprehensive view of the flux evolution during the flare.

Appendix B
VHE/X-Ray Spectral Behavior Evolution—Complementary Information and Figures

In Section 3, the NuSTAR and MAGIC spectra were fitted using a log-parabola model in which the curvature parameter β was fixed (see Equation (A1)). Given that, in such a model, the correlation between β and the spectral index α is canceled, α directly quantifies the hardness evolution. In order to determine the fixed value of β, we first ran a series of fits using a "β-free" model. We then fixed β to the average value of all time bins, yielding $\bar{\beta}_{\text{X-ray}} = 0.38$ and $\bar{\beta}_{\text{VHE}} = 0.40$ for NuSTAR and MAGIC, respectively. Figure 18 presents $\beta_{\text{X-ray}}$ versus the 3–7 keV flux (left), and β_{VHE} versus the > 400 GeV flux (right). The average is plotted with a black dashed line. For both energy ranges, β shows no clear correlation with the flux. Based on a χ^2 test, we find that, for both MAGIC and NuSTAR, the "β-fixed" model is consistent with the data within 3σ for all time bins, except two bins (out of 286) in the NuSTAR data.

For clarity purposes and to focus on the days displaying the most complex spectral behavior, the dependence of α on the flux was only shown between MJD 56393 and MJD 56399 in Section 3. We now present in Figure 19 the evolution of α for MAGIC and NuSTAR, including MJD 56400 and MJD 56401. The last two days show a significantly dimmer flux as well as a softer VHE spectrum with respect to the rest of the flare.

[56] http://fermi.gsfc.nasa.gov/ssc/data/access/lat/BackgroundModels.html
[57] https://fermi.gsfc.nasa.gov/ssc/data/analysis/

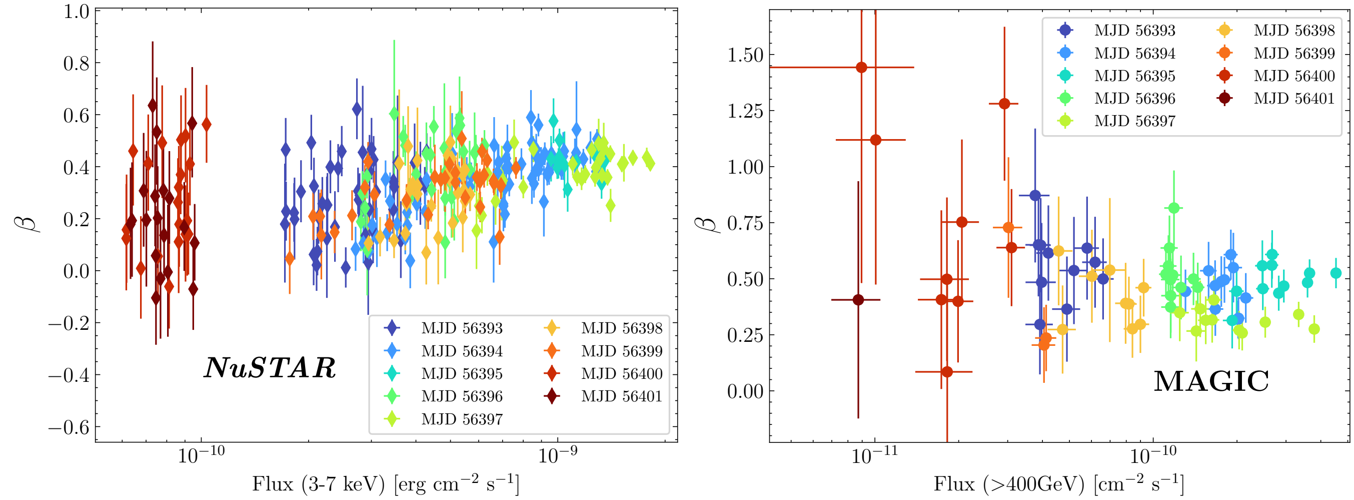

(a) (b)

Figure 18. Spectral parameter β (curvature) from log-parabola fits versus flux for (a) NuSTAR and (b) MAGIC. The spectral fits are performed in 15 minute bins for NuSTAR and 30 minute bins for MAGIC. The markers are color-coded according to the respective day of the observation.

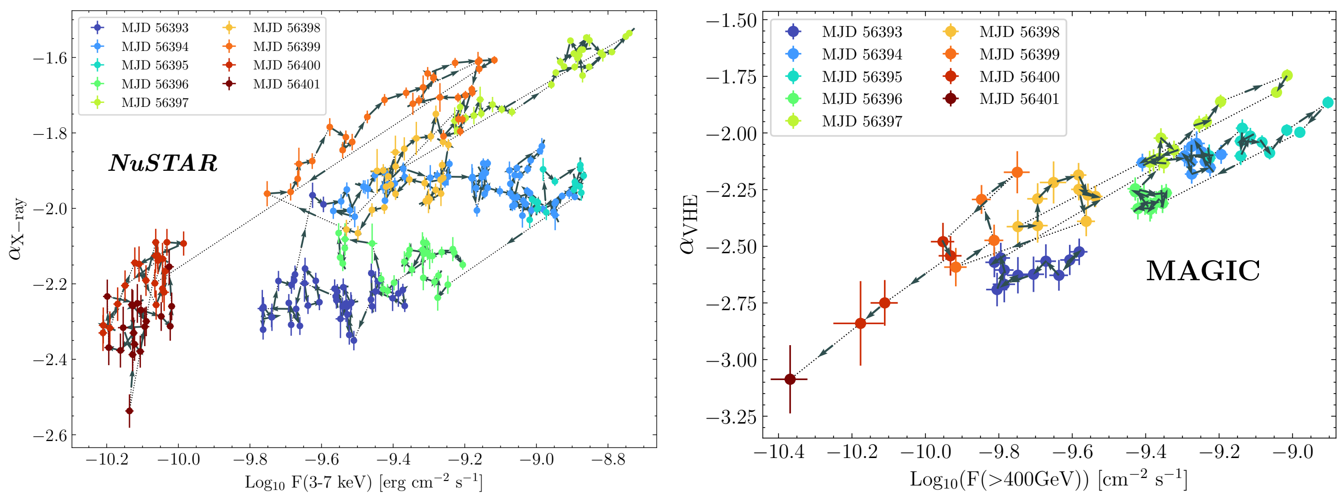

(a) (b)

Figure 19. Spectral parameter α versus flux for (a) NuSTAR and (b) MAGIC for the entire flare, up to MJD 56401. The NuSTAR fluxes are evaluated in the 3–7 keV bands, while for MAGIC they are computed above 400 GeV. The fits are performed in 15 minute bins for NuSTAR and 30 minute bins for MAGIC. The markers are color-coded according to the respective day of the observation.

Appendix C
Stationary State Modeling with Lower Doppler Factor in the "Fast" Zone

We argued in Section 4.1 that a Doppler factor of at least $\approx$100 is necessary for the "fast" component to capture the X-ray and VHE hardness during the flare. Such a Doppler factor is significantly higher than those typically adopted for Mrk 421 in the literature, which are in the range 20–40 (see, e.g., A. A. Abdo et al. 2011; M. Baloković et al. 2016). A high Doppler factor is required due to the large separation between the SED components and to overcome the Klein–Nishina effect, which softens the spectra at $\sim$TeV energies. A brief analytical justification is performed in Section 4.1. As a further illustration, we show in this section the stationary state of MJD 56393 and MJD 56395 when modeled with a "fast" zone having $\delta_{\rm fast} = 50$ and compare it with the one using $\delta_{\rm fast} = 100$.

The results are shown in Figure 20. The blue and red solid lines show the "fast" zone with $\delta_{\rm fast} = 50$ and $\delta_{\rm fast} = 100$, respectively, and the data are plotted with black markers. The model parameters for the $\delta_{\rm fast} = 100$ case are listed in Table 2. For the $\delta_{\rm fast} = 50$ case, p and R were set to the same values as in Table 2, but we modified B, l_e, $\gamma_{\rm min}$, and $\gamma_{\rm max}$, to adapt for the change in $\delta_{\rm fast}$. The corresponding parameter values are given in the caption of Figure 20. $\gamma_{\rm min}$ and $\gamma_{\rm max}$ in the $\delta_{\rm fast} = 50$ case were increased as much as the X-ray data allow, in order to describe the VHE hardness as close as possible. As one can see, the highest VHE points are underproduced even with those modifications derived with $\delta_{\rm fast} = 50$. Furthermore, in the case of MJD 56395, the inverse Compton component is narrower than that with $\delta_{\rm fast} = 100$, hence also causing some tension at the lower VHE points.

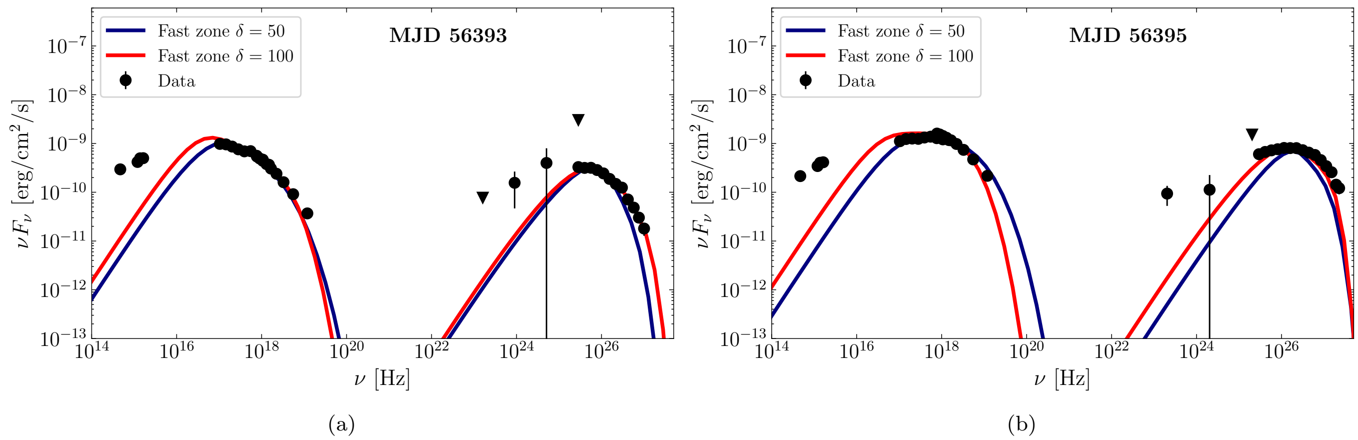

Figure 20. Comparison of the "fast" component steady state when using $\delta_{\rm fast} = 50$ and $\delta_{\rm fast} = 100$ for MJD 56393 (left) and MJD 56395 (right). The model parameters for the $\delta_{\rm fast} = 100$ case are listed in Table 2. Regarding the $\delta_{\rm fast} = 50$ case, $\log_{10} l_e = -4.9$, $\log_{10}\gamma_{\rm min} = 4.4$, $\log_{10}\gamma_{\rm min} = 5.2$, and $B = 0.37$ for MJD 56393, and $\log_{10} l_e = -4.6$, $\log_{10}\gamma_{\rm min} = 4.6$, $\log_{10}\gamma_{\rm min} = 5.5$, and $B = 0.2$ G for MJD 56395. The rest of the parameters are unchanged compared to Table 2.

Appendix D
Spatial Separation between the "Fast" and "Slow" Zones

As discussed in Section 4, our model neglects the interaction between the two emitting zones, i.e., only the synchrotron photons that are locally produced are considered for the inverse Compton process, and the electrons do not interact with the radiation field from the other zone. This simplification holds if the spatial separation between the zones is sufficiently large, in which case only the local radiation field dominates. This is particularly relevant in our case, since the relative bulk velocity of the plasma of the zones inevitably boosts the radiation density of each zone as seen in the frame of the other one.

The synchrotron energy densities from the zones in their respective comoving frames are as follows (single-primed and double-primed quantities are in the rest frame of the "slow zone" and "fast zone," respectively):

$$u'_{\rm syn,slow} \approx \frac{\nu_{\rm p,slow} L^{\rm obs}_{\rm syn,slow}(\nu_{\rm p,slow})}{4\pi c R^2_{\rm slow}\delta^4_{\rm slow}} \tag{D1}$$

$$u''_{\rm syn,fast} \approx \frac{\nu_{\rm p,fast} L^{\rm obs}_{\rm syn,fast}(\nu_{\rm p,fast})}{4\pi c R^2_{\rm fast}\delta^4_{\rm fast}}, \tag{D2}$$

where $L^{\rm obs}_{\rm syn}(\nu_{\rm p})$ is the observed synchrotron luminosity at the peak frequency $\nu_{\rm p}$. Assuming that the plasma in the two components travels on the same axis (parallel to the jet), the relative bulk velocity and Lorentz factors are

$$\beta_{\rm rel} = \frac{\beta_{\rm slow} - \beta_{\rm fast}}{1 - \beta_{\rm fast}\beta_{\rm slow}} \tag{D3}$$

$$\Gamma_{\rm rel} = \Gamma_{\rm b,fast}\Gamma_{\rm b,slow}(1 - \beta_{\rm fast}\beta_{\rm slow}). \tag{D4}$$

Our model uses $\delta_{\rm b,fast} = 100$ and $\delta_{\rm slow} = 30$, which implies $\Gamma_{\rm b,fast} = 100$ and $\Gamma_{\rm b,slow} = 15$ in the case that the viewing angle relative to the jet's axis is $\Theta = 1/\Gamma_{\rm fast}$. With these choice of parameters, $\beta_{\rm rel} = -0.95$ and $\Gamma_{\rm rel} = 3.4$.

Following M. Petropoulou (2014), the radiation of the "slow zone" as observed in the comoving frame of the "fast zone" is given by

$$\begin{aligned} u''_{\rm syn,slow} &= \frac{u'_{\rm syn,slow}}{2}\Gamma^2_{\rm rel}\int_{\mu_0}^{1} d\mu'(1 - \beta_{\rm rel}\mu')^2 \\ &= \frac{u'_{\rm syn,slow}}{2}\Gamma^2_{\rm rel}\Bigg(1 - \mu_0 - \beta_{\rm rel}(1 - \mu_0^2) \\ &\quad + \frac{\beta^2_{\rm rel}}{3}(1 - \mu_0^3)\Bigg), \end{aligned} \tag{D5}$$

where $\mu_0 = r_0/\sqrt{r_0^2 + R^2_{\rm slow}}$, with r_0 being the separation between the two regions.

Requiring $u''_{\rm syn,slow} < 0.1\, u''_{\rm syn,fast}$ ensures that the synchrotron photon field of the "slow zone" entering the "fast zone" is largely subdominant with respect to one being locally produced. This condition translates into a lower limit $r_0 > 1.5 \times 10^{17}$ cm using the parameters of Table 2. Repeating the above exercise but for the "slow zone", i.e., finding the minimal r_0 for which $u'_{\rm syn,fast} < 0.1\, u'_{\rm syn,slow}$, yields $r_0 > 0.9 \times 10^{15}$ cm. We thus conclude that neglecting the interaction holds in a realistic configuration where the two regions are separated by a few 10^{17} cm, equivalent to $\sim 10^{-1}$ pc, orders of magnitude smaller than the jet's size.

Appendix E
Determination of the Time Evolution Curve of the Power-law Slope for the Injected Electrons in the "Fast" Zone

Using the X-ray observations, we determine the time evolution of the power-law slope p of the electrons (injected inside the "fast" zone). The synchrotron nature of the X-ray photons allows, in principle, a direct prediction of the electron distribution slope based on the NuSTAR best-fit spectral model. We find, however, that the NuSTAR indices (in the 3–30 keV band) are significantly softer than the ones measured with Swift-XRT in simultaneous time bins (in the 0.3–10 keV band). It indicates that NuSTAR covers (at least partially) a high-energy cutoff in the electron spectrum (or is probing a radiative cooling break). Hence, the NuSTAR photon indices alone prevent us to properly constrain the uncooled electron distribution (or well below the high-energy cutoff) injected in the "fast" zone. The photon indices determined closer to the Swift-XRT band are required for the modeling. We stress that, in our scenario, the "fast" zone dominates not only in the NuSTAR range, but also in the Swift-XRT band. Unfortunately, the poor temporal sampling from Swift-XRT throughout the flare compared to NuSTAR does not allow a determination of the evolution of the X-ray photon index on 15 minute timescales down to the 0.3–10 keV band.

In order to address that issue, we first perform a series of spectral fits in each of the NuSTAR 15 minute time bins (following the same data reduction recipe described in Section 2), as well as in all available Swift-XRT observations assuming a simple power-law model ($dN/dE \propto E^{-\Gamma_{\text{X-ray}}}$). In a second step, we correlate the NuSTAR and Swift-XRT slopes using strictly simultaneous measurements. This allows us to find an empirical, linear relationship between the indices of the two instruments. We used the obtained best-fit linear relation to convert all the NuSTAR photon indices obtained in 15 minute bins into a photon index "light curve" as it would be measured in the Swift-XRT band. Finally, this synthetic photon index light curve ($\Gamma_{\text{X-ray,synthetic}}(t)$) is transformed into a time evolution curve of the electron power-law slope $p(t)$ using the well-known relationship for synchrotron emission (G. B. Rybicki & A. P. Lightman 1979):

$$\Gamma_{\text{X-ray,synthetic}}(t) = \frac{p(t) + 1}{2}, \tag{E1}$$

where $\Gamma_{\text{X-ray}}$ is the photon power-law index and p the electron slope. We highlight that, although a log-parabola model is significantly preferred in general to describe the NuSTAR and Swift-XRT spectra (see Section 3), our aim here is not to characterize with accuracy the X-ray data, but to obtain an estimate of the injected electron power-law slope using Equation (E1). Having a preliminary $p(t)$ evolution curve, we apply some final fine-tuning by hand (at the level of 10% at most) to optimize the data/model match in the modeling process. Finally, we apply some Gaussian smoothing on MJD 56393 and MJD 56394, in order to remove a few statistical fluctuations in the measured photon index that led to artificial short-timescale variations in $p(t)$ and thus also in the model fluxes. The other days did not require such smoothing, so we have left them untouched. The final $p(t)$ curve used for the model is shown with black markers in Figure 7.

Appendix F
Snapshot of the Time-dependent Model SEDs

As illustrative examples, we present the SED model in one of the 15 minute intervals of each day. They are shown in Figures 21 and 22. The complete set of SEDs is published as online material, and can be retrieved from the Zenodo repository DOI: 10.5281/zenodo.17054582.

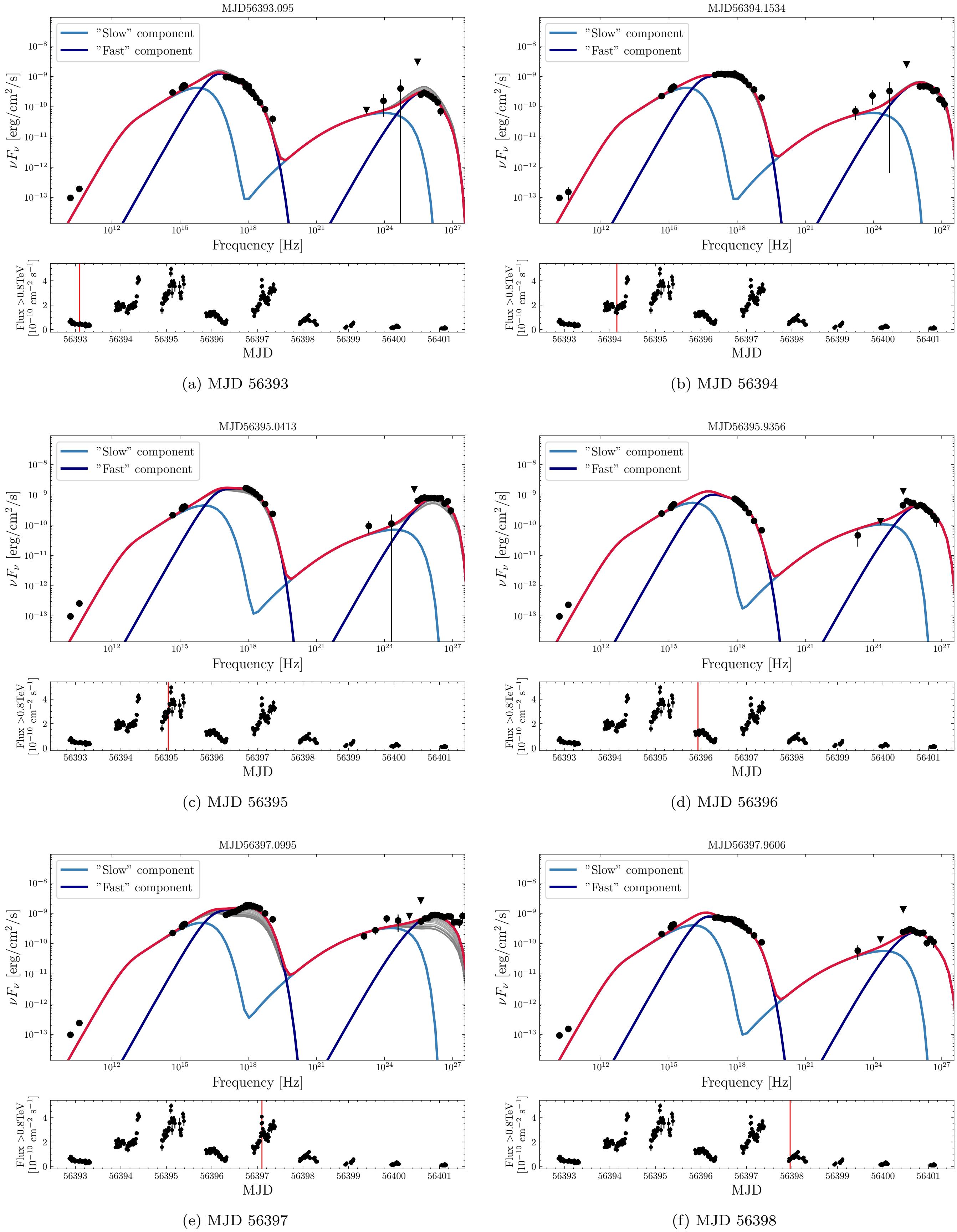

Figure 21. Snapshots from the time-dependent model in one of the 15 minute intervals of each day. The light blue line represents the emission from the "fast" zone, the dark blue line is the emission from the "slow" zone, and the solid red line is the sum of the two components. Data are depicted with dark points. We show with gray lines the model curves up to 80 light-crossing time prior to the time of each snapshot, to illustrate the variability.

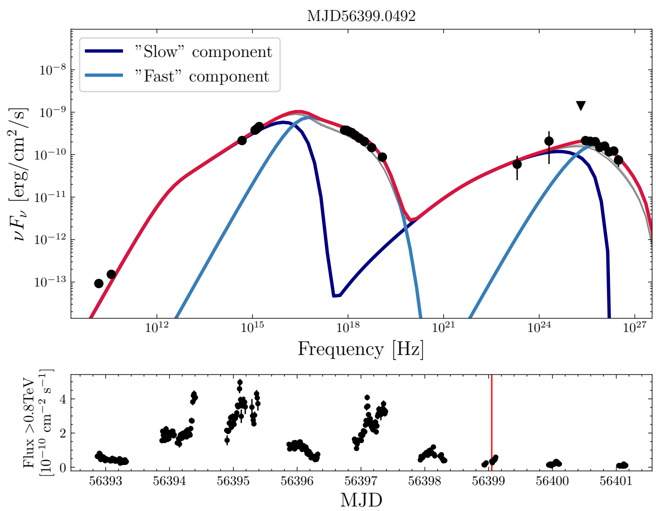

(g) MJD 56399

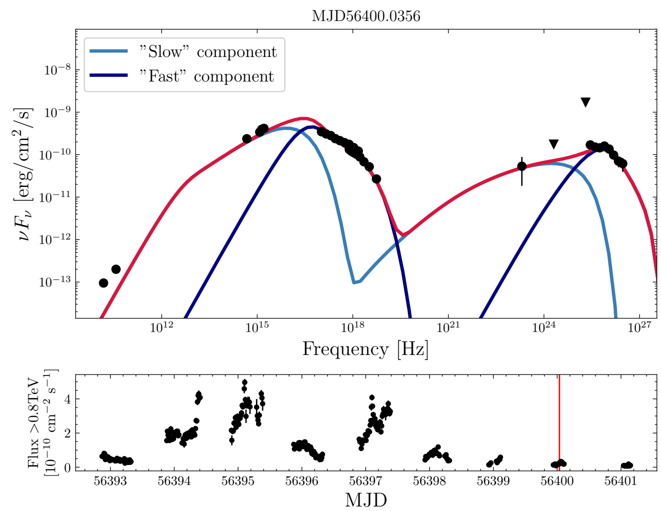

(h) MJD 56400

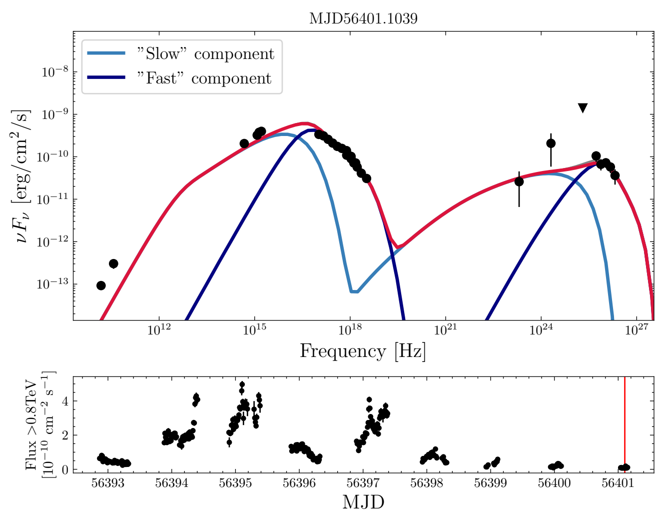

(i) MJD 56401

Figure 22. Same as Figure 21, for the last three days of the 9 day outburst (MJD 56399–56401).

ORCID iDs

S. Abe https://orcid.org/0000-0001-7250-3596
J. Abhir https://orcid.org/0000-0001-8215-4377
A. Abhishek https://orcid.org/0009-0005-5239-7905
A. Aguasca-Cabot https://orcid.org/0000-0001-8816-4920
I. Agudo https://orcid.org/0000-0002-3777-6182
S. Ansoldi https://orcid.org/0000-0002-5613-7693
L. A. Antonelli https://orcid.org/0000-0002-5037-9034
A. Arbet Engels https://orcid.org/0000-0001-9076-9582
C. Arcaro https://orcid.org/0000-0002-1998-9707
A. Babić https://orcid.org/0000-0002-1444-5604
C. Bakshi https://orcid.org/0009-0007-1843-5386
U. Barres de Almeida https://orcid.org/0000-0001-7909-588X
J. A. Barrio https://orcid.org/0000-0002-0965-0259
L. Barrios-Jiménez https://orcid.org/0009-0008-6006-175X
I. Batković https://orcid.org/0000-0002-1209-2542
J. Becerra González https://orcid.org/0000-0002-6729-9022
W. Bednarek https://orcid.org/0000-0003-0605-108X
E. Bernardini https://orcid.org/0000-0003-3108-1141
A. Berti https://orcid.org/0000-0003-0396-4190
C. Bigongiari https://orcid.org/0000-0003-3293-8522
A. Biland https://orcid.org/0000-0002-1288-833X
O. Blanch https://orcid.org/0000-0002-8380-1633
G. Bonnoli https://orcid.org/0000-0003-2464-9077
Ž. Bošnjak https://orcid.org/0000-0001-6536-0320
E. Bronzini https://orcid.org/0000-0001-8378-4303
I. Burelli https://orcid.org/0000-0002-8383-2202
A. Campoy-Ordaz https://orcid.org/0000-0001-9352-8936
A. Carosi https://orcid.org/0000-0001-8690-6804
R. Carosi https://orcid.org/0000-0002-4137-4370
M. Carretero-Castrillo https://orcid.org/0000-0002-1426-1311
A. J. Castro-Tirado https://orcid.org/0000-0002-0841-0026
D. Cerasole https://orcid.org/0000-0003-2033-756X
G. Ceribella https://orcid.org/0000-0002-9768-2751
Y. Chai https://orcid.org/0000-0003-2816-2821
A. Cifuentes https://orcid.org/0000-0003-1033-5296
J. L. Contreras https://orcid.org/0000-0001-7282-2394
J. Cortina https://orcid.org/0000-0003-4576-0452
S. Covino https://orcid.org/0000-0001-9078-5507
F. D'Ammando https://orcid.org/0000-0001-7618-7527
P. Da Vela https://orcid.org/0000-0003-0604-4517

F. Dazzi https://orcid.org/0000-0001-5409-6544
A. De Angelis https://orcid.org/0000-0002-3288-2517
B. De Lotto https://orcid.org/0000-0003-3624-4480
J. Delgado https://orcid.org/0000-0002-0166-5464
C. Delgado Mendez https://orcid.org/0000-0002-7014-4101
F. Di Pierro https://orcid.org/0000-0003-4861-432X
R. Di Tria https://orcid.org/0009-0007-1088-5307
L. Di Venere https://orcid.org/0000-0003-0703-824X
D. Dominis Prester https://orcid.org/0000-0002-9880-5039
A. Donini https://orcid.org/0000-0002-3066-724X
D. Dorner https://orcid.org/0000-0001-8823-479X
M. Doro https://orcid.org/0000-0001-9104-3214
D. Elsaesser https://orcid.org/0000-0001-6796-3205
J. Escudero https://orcid.org/0000-0002-4131-655X
L. Fariña https://orcid.org/0000-0003-4116-6157
L. Foffano https://orcid.org/0000-0002-0709-9707
L. Font https://orcid.org/0000-0003-2109-5961
Y. Fukazawa https://orcid.org/0000-0002-0921-8837
R. J. García López https://orcid.org/0000-0002-8204-6832
M. Garczarczyk https://orcid.org/0000-0002-0445-4566
S. Gasparyan https://orcid.org/0000-0002-0031-7759
J. G. Giesbrecht Paiva https://orcid.org/0000-0002-5817-2062
N. Giglietto https://orcid.org/0000-0002-9021-2888
F. Giordano https://orcid.org/0000-0002-8651-2394
P. Gliwny https://orcid.org/0000-0002-4183-391X
T. Gradetzke https://orcid.org/0000-0003-0646-2495
R. Grau https://orcid.org/0000-0002-1891-6290
D. Green https://orcid.org/0000-0003-0768-2203
J. G. Green https://orcid.org/0000-0002-1130-6692
A. Hahn https://orcid.org/0000-0003-0827-5642
T. Hassan https://orcid.org/0000-0002-4758-9196
L. Heckmann https://orcid.org/0000-0002-6653-8407
J. Herrera Llorente https://orcid.org/0000-0002-3771-4918
D. Hrupec https://orcid.org/0000-0002-7027-5021
D. Israyelyan https://orcid.org/0000-0002-5804-6605
J. Jahanvi https://orcid.org/0000-0002-7217-0821
I. Jiménez Martínez https://orcid.org/0000-0003-2150-6919
J. Jormanainen https://orcid.org/0000-0003-4519-7751
T. Kayanoki https://orcid.org/0000-0002-6960-9274
P. M. Kouch https://orcid.org/0000-0002-9328-2750
H. Kubo https://orcid.org/0000-0001-9159-9853
J. Kushida https://orcid.org/0000-0002-8002-8585
M. Láinez https://orcid.org/0000-0003-3848-922X
A. Lamastra https://orcid.org/0000-0003-2403-913X
E. Lindfors https://orcid.org/0000-0002-9155-6199
S. Lombardi https://orcid.org/0000-0002-6336-865X
F. Longo https://orcid.org/0000-0003-2501-2270
M. López-Moya https://orcid.org/0000-0002-8791-7908
A. López-Oramas https://orcid.org/0000-0003-4603-1884
S. Loporchio https://orcid.org/0000-0003-4457-5431
P. Majumdar https://orcid.org/0000-0002-5481-5040
M. Makariev https://orcid.org/0000-0002-1622-3116
M. Mallamaci https://orcid.org/0000-0003-4068-0496
G. Maneva https://orcid.org/0000-0002-5959-4179
M. Manganaro https://orcid.org/0000-0003-1530-3031
S. Mangano https://orcid.org/0000-0001-5872-1191
K. Mannheim https://orcid.org/0000-0002-2950-6641
S. Marchesi https://orcid.org/0000-0001-5544-0749
M. Mariotti https://orcid.org/0000-0003-3297-4128
M. Martínez https://orcid.org/0000-0002-9763-9155
P. Maruševec https://orcid.org/0000-0002-6748-4615
D. Miceli https://orcid.org/0000-0002-2686-0098
J. M. Miranda https://orcid.org/0000-0002-1472-9690
R. Mirzoyan https://orcid.org/0000-0003-0163-7233
E. Molina https://orcid.org/0000-0003-1204-5516
H. A. Mondal https://orcid.org/0000-0001-7217-0234
A. Moralejo https://orcid.org/0000-0002-1344-9080
C. Nanci https://orcid.org/0000-0002-1791-8235
V. Neustroev https://orcid.org/0000-0003-4772-595X
M. Nievas Rosillo https://orcid.org/0000-0002-8321-9168
C. Nigro https://orcid.org/0000-0001-8375-1907
S. Nozaki https://orcid.org/0000-0002-6246-2767
A. Okumura https://orcid.org/0000-0002-3055-7964
J. Otero-Santos https://orcid.org/0000-0002-4241-5875
S. Paiano https://orcid.org/0000-0002-2239-3373
D. Paneque https://orcid.org/0000-0002-2830-0502
R. Paoletti https://orcid.org/0000-0003-0158-2826
J. M. Paredes https://orcid.org/0000-0002-1566-9044
M. Peresano https://orcid.org/0000-0002-7537-7334
M. Persic https://orcid.org/0000-0003-1853-4900
F. Podobnik https://orcid.org/0000-0001-6125-9487
P. G. Prada Moroni https://orcid.org/0000-0001-9712-9916
E. Prandini https://orcid.org/0000-0003-4502-9053
W. Rhode https://orcid.org/0000-0003-2636-5000
M. Ribó https://orcid.org/0000-0002-9931-4557
J. Rico https://orcid.org/0000-0003-4137-1134
N. Sahakyan https://orcid.org/0000-0003-2011-2731
F. G. Saturni https://orcid.org/0000-0002-1946-7706
K. Schmitz https://orcid.org/0000-0002-9883-4454
F. Schmuckermaier https://orcid.org/0000-0003-2089-0277
A. Simongini https://orcid.org/0009-0000-3416-9865
J. Sitarek https://orcid.org/0000-0002-1659-5374
V. Sliusar https://orcid.org/0000-0002-4387-9372
D. Sobczynska https://orcid.org/0000-0003-4973-7903
A. Stamerra https://orcid.org/0000-0002-9430-5264
J. Strišković https://orcid.org/0000-0003-2902-5044
D. Strom https://orcid.org/0000-0003-2108-3311
M. Strzys https://orcid.org/0000-0001-5049-1045
Y. Suda https://orcid.org/0000-0002-2692-5891
R. Takeishi https://orcid.org/0000-0001-6335-5317
F. Tavecchio https://orcid.org/0000-0003-0256-0995
T. Terzić https://orcid.org/0000-0002-4209-3407
A. Tutone https://orcid.org/0000-0002-2840-0001
S. Ubach https://orcid.org/0000-0002-6159-5883
J. van Scherpenberg https://orcid.org/0000-0002-6173-867X
M. Vazquez Acosta https://orcid.org/0000-0002-2409-9792
S. Ventura https://orcid.org/0000-0001-7065-5342
I. Viale https://orcid.org/0000-0001-5031-5930
C. F. Vigorito https://orcid.org/0000-0002-0069-9195
V. Vitale https://orcid.org/0000-0001-8040-7852
I. Vovk https://orcid.org/0000-0003-3444-3830
R. Walter https://orcid.org/0000-0003-2362-4433
F. Wersig https://orcid.org/0009-0006-1828-6117
M. Will https://orcid.org/0000-0002-7504-2083
T. Yamamoto https://orcid.org/0000-0001-9734-8203
M. Petropoulou https://orcid.org/0000-0001-6640-0179
M. Polkas https://orcid.org/0000-0002-8889-2167
A. Mastichiadis https://orcid.org/0000-0001-5217-4801

References

Abdo, A. A., Ackermann, M., Agudo, I., et al. 2010, ApJ, 716, 30
Abdo, A. A., Ackermann, M., Ajello, M., et al. 2011, ApJ, 736, 131
Abeysekara, A. U., Archambault, S., Archer, A., et al. 2017, ApJ, 834, 2
Acciari, V. A., Ansoldi, S., Antonelli, L. A., et al. 2020a, ApJS, 248, 29
Acciari, V. A., Ansoldi, S., Antonelli, L. A., et al. 2020b, ApJS, 247, 16
Acciari, V. A., Ansoldi, S., Antonelli, L. A., et al. 2021, MNRAS, 504, 1427

Acciari, V. A., Arlen, T., Aune, T., et al. 2014, APh, 54, 1
Ackermann, M., Ajello, M., Albert, A., et al. 2012, ApJS, 203, 4
Albert, J., Aliu, E., Anderhub, H., et al. 2008, ApJ, 674, 1037
Aleksić, J., Ansoldi, S., Antonelli, L. A., et al. 2016, APh, 72, 76
Arnaud, K. A. 1996, ASPC, 101, 17
Atwood, W. B., Abdo, A. A., Ackermann, M., et al. 2009, ApJ, 697, 1071
Baheeja, C., Sahayanathan, S., Rieger, F. M., & Ravikumar, C. D. 2024, PhRvD, 109, 103039
Baloković, M., Paneque, D., Madejski, G., et al. 2016, ApJ, 819, 156
Becker, P. A., Le, T., & Dermer, C. D. 2006, ApJ, 647, 539
Begelman, M. C., Blandford, R. D., & Rees, M. J. 1984, RvMP, 56, 255
Benbow, W. & VERITAS Collaboration 2017, ICRC, 35, 641
Blumenthal, G. R., & Gould, R. J. 1970, RvMP, 42, 237
Burrows, D. N., Hill, J. E., Nousek, J. A., et al. 2005, SSRv, 120, 165
Carnerero, M. I., Raiteri, C. M., Villata, M., et al. 2017, MNRAS, 472, 3789
Daly, R. A., & Marscher, A. P. 1988, ApJ, 334, 539
Domínguez, A., Primack, J. R., Rosario, D. J., et al. 2011, MNRAS, 410, 2556
Donath, A., Terrier, R., Remy, Q., et al. 2023, A&A, 678, A157
Falcone, A. D., Cui, W., & Finley, J. P. 2004, ApJ, 601, 165
Franceschini, A., & Rodighiero, G. 2018, A&A, 614, C1
Franceschini, A., Rodighiero, G., & Vaccari, M. 2008, A&A, 487, 837
Georganopoulos, M., & Kazanas, D. 2003, ApJL, 594, L27
Ghisellini, G., Tavecchio, F., & Chiaberge, M. 2005, A&A, 432, 401
Giannios, D. 2013, MNRAS, 431, 355
Giannios, D., Uzdensky, D. A., & Begelman, M. C. 2009, MNRAS, 395, L29
Gilmore, R. C., Somerville, R. S., Primack, J. R., & Domínguez, A. 2012, MNRAS, 422, 3189
H. E. S. S. Collaboration, Abdalla, H., Adam, R., et al. 2020, A&A, 633, A162
H. E. S. S. Collaboration, Abramowski, A., Acero, F., et al. 2012, A&A, 539, A149
Harrison, F. A., Craig, W. W., Christensen, F. E., et al. 2013, ApJ, 770, 103
Hervet, O., Williams, D. A., Falcone, A. D., & Kaur, A. 2019, ApJ, 877, 26
Holder, J., Acciari, V. A., Aliu, E., et al. 2008, AIP, 1085, 657
Homan, D. C., Cohen, M. H., Hovatta, T., et al. 2021, ApJ, 923, 67
Jormanainen, J., Hovatta, T., Christie, I. M., et al. 2023, A&A, 678, A140
Kalberla, P. M. W., Burton, W. B., Hartmann, D., et al. 2005, A&A, 440, 775
Kapanadze, B., Dorner, D., Vercellone, S., et al. 2016, ApJ, 831, 102
Katarzyński, K., Ghisellini, G., Tavecchio, F., et al. 2005, A&A, 433, 479
Keshet, U., & Waxman, E. 2005, PhRvL, 94, 111102
Kirk, J. G., & Duffy, P. 1999, JPhG, 25, R163
Kirk, J. G., Rieger, F. M., & Mastichiadis, A. 1998, A&A, 333, 452
Krawczynski, H., Hughes, S. B., Horan, D., et al. 2004, ApJ, 601, 151
Lister, M. L., Aller, M. F., Aller, H. D., et al. 2016, AJ, 152, 12
Madsen, K. K., Forster, K., Grefenstette, B. W., Harrison, F. A., & Miyasaka, H. 2022, JATIS, 8, 034003
MAGIC Collaboration, Acciari, V. A., Ansoldi, S., et al. 2020, A&A, 637, A86
MAGIC Collaboration, Acciari, V. A., Ansoldi, S., et al. 2021a, A&A, 655, A89
MAGIC Collaboration, Acciari, V. A., Ansoldi, S., et al. 2021b, A&A, 647, A163
Mannheim, K. 1993, A&A, 269, 67
Maraschi, L., Ghisellini, G., & Celotti, A. 1992, ApJL, 397, L5
Mastichiadis, A., & Kirk, J. G. 1995, A&A, 295, 613
Mastichiadis, A., & Kirk, J. G. 1997, A&A, 320, 19
Mattox, J. R., Bertsch, D. L., Chiang, J., et al. 1996, ApJ, 461, 396
Mücke, A., & Protheroe, R. J. 2001, APh, 15, 121
Paliya, V. S., Böttcher, M., Diltz, C., et al. 2015, ApJ, 811, 143
Petropoulou, M. 2014, A&A, 571, A83
Petropoulou, M., Giannios, D., & Sironi, L. 2016, MNRAS, 462, 3325
Petropoulou, M., & Sironi, L. 2018, MNRAS, 481, 5687
Pian, E., Vacanti, G., Tagliaferri, G., et al. 1998, ApJL, 492, L17
Polkas, M., Petropoulou, M., Vasilopoulos, G., et al. 2021, MNRAS, 505, 6103
Raiteri, C. M., Villata, M., Acosta-Pulido, J. A., et al. 2017, Natur, 552, 374
Raiteri, C. M., Villata, M., Larionov, V. M., et al. 2007, A&A, 473, 819
Ravasio, M., Tagliaferri, G., Ghisellini, G., & Tavecchio, F. 2004, A&A, 424, 841
Roming, P. W. A., Kennedy, T. E., Mason, K. O., et al. 2005, SSRv, 120, 95
Rybicki, G. B., & Lightman, A. P. 1979, Radiative Processes in Astrophysics (Wiley)
Sato, R., Kataoka, J., Takahashi, T., et al. 2008, AIP, 1085, 447
Sikora, M., Madejski, G., Moderski, R., & Poutanen, J. 1997, ApJ, 484, 108
Sironi, L., Giannios, D., & Petropoulou, M. 2016, MNRAS, 462, 48
Sironi, L., & Spitkovsky, A. 2014, ApJL, 783, L21
Takahashi, T., Tashiro, M., Madejski, G., et al. 1996, ApJL, 470, L89
Tavecchio, F., & Ghisellini, G. 2016, MNRAS, 456, 2374
Tavecchio, F., Maraschi, L., & Ghisellini, G. 1998, ApJ, 509, 608
Ulrich, M. H., Kinman, T. D., Lynds, C. R., Rieke, G. H., & Ekers, R. D. 1975, ApJ, 198, 261
Villata, M., Raiteri, C. M., Balonek, T. J., et al. 2006, A&A, 453, 817
Villata, M., Raiteri, C. M., Gurwell, M. A., et al. 2009, A&A, 504, L9
Villata, M., Raiteri, C. M., Kurtanidze, O. M., et al. 2002, A&A, 390, 407
Villata, M., Raiteri, C. M., Larionov, V. M., et al. 2008, A&A, 481, L79
Virtanen, J. J. P., & Vainio, R. 2005, A&A, 439, 461
Werner, G. R., Uzdensky, D. A., Cerutti, B., Nalewajko, K., & Begelman, M. C. 2016, ApJL, 816, L8
Zanin, R., Carmona, E., Sitarek, J., et al. 2013, ICRC, 33, 2937
Zech, A., & Lemoine, M. 2021, A&A, 654, A96
Zhang, Y. H., Treves, A., Celotti, A., et al. 2002, ApJ, 572, 762
Zirakashvili, V. N., & Aharonian, F. 2007, A&A, 465, 695